

MODEL BASED ANALYSIS OF MULTIMODAL
NEUROIMAGING: FROM NEURAL MASSES TO
SPECTRAL GRAPH THEORY

A Dissertation

Presented to the Faculty of the Weill Cornell

Graduate School of Medical Sciences

in Partial Fulfillment of the Requirements for the Degree of

Doctor of Philosophy

by

Xihe Xie

November 2021

© 2021 Xihe Xie

ALL RIGHTS RESERVED

MODEL BASED ANALYSIS OF MULTIMODAL NEUROIMAGING: FROM
NEURAL MASSES TO SPECTRAL GRAPH THEORY

Xihe Xie, Ph.D.

Cornell University 2021

The direct link between human neurobiology and observed brain dynamics drives fundamental research efforts in neuroscience. How does functional brain patterns arise from the underlying anatomy? Alongside technological advances, multimodal brain imaging enlarged the coverage of observable brain characteristics, and data-driven network theoretics emerged as a valuable framework for understanding large datasets and building biophysically based models of brain structure and function. This dissertation explores structure function models of different complexity and spatiotemporal scale, utilizing tools from signal processing, dynamical systems, optimization, and stochastic processes.

With diffusion imaging derived white matter streamlines, we built whole brain networks describing the underlying anatomical connections of the brain. The combination of connection strengths and inter-region delays provided anatomical networks that were rich in information. We showcase linear, low dimensional and highly interpretable network models of brain function that fully utilizes the brain's anatomical connectivity. Moreover, we found these models to capture the spatial patterns of brain activity in addition to observed functional patterns of the brain. We also examine a non-linear neural mass model of neuronal mean-field oscillations, in order to determine how parameterization and model complexity dictate model performance.

This document is dedicated to all Cornell graduate students.

ACKNOWLEDGEMENTS

The author wishes to acknowledge the generous contribution of several individuals and organizations that have made this dissertation possable. Foremost is Dr. Ashish Raj and Dr. Srikantan Nagarajan, two advisors that provided opportunities and countless valuable advice from Weill Cornell to UCSF.

The Neuroscience Department at Weill Cornell Graduate School for providing a welcoming community and outstanding opportunities for teaching and peer led leaerning. UCSF's Open Science Group, the Brainhack community, and Neurohackademy kept me energized and shared valuable knowledge in scientific knowledge, publishing, ethics, and data practices. The ReproNim team, INCF, and the ReproNim Fellowship trainers and trainees. Finally, many scientists and friends have given selflessly their expertise and support, including:

TABLE OF CONTENTS

Dedication	4
Acknowledgements	5
Table of Contents	6
List of Tables	8
List of Figures	9
1 Introduction	1
2 Advances in Diffusion MRI	3
2.1 Diffusion MRI Processing	3
2.2 DESIGNER	4
2.3 GPU-accelerated Diffusion MRI Tractography in DIPY	4
2.3.1 Methods	4
2.3.2 Results	5
2.3.3 Discussion and Conclusion	5
3 Emergence of Canonical Functional Networks from the Structural Connectome	8
3.1 Introduction	8
3.2 Theory	12
3.2.1 Network Diffusion of Brain Activity	12
3.2.2 Complex Laplacian Matrix	14
4 Spectral Graph Theory of Brain Oscillations	16
4.1 Introduction	16
4.1.1 The Structure-Function Problem in Neuroscience	16
4.1.2 A hierarchical, analytic, low-dimensional and linear spectral graph theoretic model of brain oscillations	19
4.2 Methods	20
4.2.1 Spectral graph model development	20
4.2.2 Macroscopic scale: signal evolution on the entire graph . .	26
4.2.3 Experimental Procedures	29
4.2.4 Data Processing	30
4.2.5 Model Optimization	33
4.3 Results	34
4.3.1 Graph Laplacian eigenmodes mediate a diversity of frequency responses	34
4.3.2 Spectral distribution of MEG power depends on model parameters but not connectivity	37
4.3.3 Spectral graph model recapitulates the spatial distribution of MEG power	41
4.4 Discussion	47

4.4.1	Recapitulating regional power spectra at all frequencies	48
4.4.2	Revealing sources of heterogeneity in spatial patterns of brain activity	49
4.4.3	Macroscopic brain rhythms are governed by the connectome	49
4.4.4	Emergence of linearity from chaotic brain dynamics	51
4.4.5	Relationship to other work	52
4.4.6	Other limitations and extensions	54
4.4.7	Potential applications	54
5	Chapter 3	56
6	Chapter 4	57
A	Chapter 1 of appendix	58
	Bibliography	59

LIST OF TABLES

4.1 SGM parameters values and limits	22
--	----

LIST OF FIGURES

2.1	For the same task (HARDI data, 27 seeds per WM voxel) tractography duration decreases with the number of GPUs available. Speedup relative to CPU ranges from approximately 200-fold, with one GPU to almost 700-fold with 8 GPUs.	6
2.2	GPU-accelerated tractography of high-resolution data, acquired at 0.625 mm ³ effective resolution. This is a small subset sampled randomly for visualization purposes: approximately 8M streamlines of the 150M streamlines tracked.	7
3.1	The analysis overview. Structural connectivity matrix (C) and distance adjacency matrix (D) were extracted from diffusion MRI derived tractograms, to construct the complex Laplacian of the brain's structural network. An eigen decomposition on the network's complex Laplacian (\mathcal{L}) was performed obtain complex structural eigenmodes of the brain (U). The spatial similarities were computed between the structural eigenmodes and canonical functional networks in fMRI. Here, as an example, we show brain rendering of the leading eigenmode from the HCP template structural connectome (right column, top) and the canonical visual functional network (right column, bottom).	15

- 4.1 The linearized spectral graph model. (a) Conventional neural mass models instantiate a large assembly of excitatory and inhibitory neurons, which are modeled as fully connected internally. External inputs and outputs are gated through the excitatory neurons only, and inhibitory neurons are considered strictly local. The proposed linear model condenses these local assemblies into lumped linear systems $f_e(t)$ and $f_i(t)$, Gamma-shaped functions having time constants τ_e and τ_i (see panel (b)). The recurrent architecture of the two pools within a local area is captured by the gain terms g_{ee} , g_{ii} , g_{ei} , parameterizing the recurrents within excitatory, inhibitory and cross-populations. (c) The absolute value of eigenvalues of the complex Laplacian $\mathcal{L}(\omega)$ are plotted against the eigenvector index. Each dot represents one eigenvalue $\lambda(\omega)$; its color represents the frequency ω - low (blue) to high (yellow). These eigenvalues change by frequency; small eigenvalues change more compared to large ones. (d) Frequency response of each eigenmode plotted on the complex plane with default model parameters and a template structural connectome. Each curve represents the transit in the complex plane of a single eigenmode's frequency response, starting at low frequencies in the bottom right quadrant, and moving to the upper left quadrant at high frequencies. The magnitude of the response, given by the distance from the origin, suggests that most eigenmodes have two prominent lobes, roughly corresponding to lower frequency alpha rhythms and higher frequency gamma rhythms. In contrast, the lowest eigenmodes start off far from the origin, indicative of a low-pass response. (e) Magnitude of the frequency response of each eigenmode reinforces these impressions more clearly, with clear alpha peak, as well as slower rhythms. (f) The spatial patterns of the top 5 eigenmodes of $\mathcal{L}(\omega)$, evaluated at the alpha frequency. The first 5 eigenmodes $u_1 \dots u_5$ produce resting-state functional networks patterns; These patterns are not exclusive and greatly depend on the frequency, model parameters, and the connectome.

21

4.2	Spectral graph model spectra for one subject. Top-Source localized MEG power spectrum for 68 parcellated brain regions. Estimated spectra for each brain region are shown in blue, and average spectrum across all regions is shown in black. The subsequent rows show each eigenmode's spectral magnitude response with model parameters optimized to match the MEG spectrum ($\tau_e = 0.0073$, $\tau_i = 0.0085$, $\tau_G = 0.0061$, $g_{ei} = 2.9469$, $g_{ii} = 4.4865$, $v = 18.3071$, and $\alpha = 0.4639$). Left column shows each eigenmode's frequency responses, while the right column shows the same information as heatmaps. (a) Model using subject's individual structural connectome. (b) Model using average template connectome obtained from 80 HCP subjects. (c) Model using uniform connectivity matrix of ones. (d) Model using randomized connectivity matrix with 75% sparsity. (f) Model using randomized connectivity matrix with 95% sparsity.	36
4.3	Spectral graph model depicts MEG spectra. (a) The observed spectra and SGM's simulated spectra for four representative subjects. Red and cyan curves illustrate source localized empirical average spectra and region-wise spectra respectively. Black and blue curves illustrate simulated average spectra and region-wise spectra respectively. (b) Average observed spectrum across subjects is shown in red. Subsequently, we show average simulated spectra with optimized parameters for individual subject connectomes (black), HCP template connectome (purple), 80% sparse distance connectome (blue), 80% sparse random connectome (green). As a comparison, we also show simulated spectrum with a network neural mass model (pink) and average parameter values and individual connectome (green).	38
4.4	Spectral graph model parameter optimization. (a) Distribution of optimized model parameter values across all 36 subjects for parameters $\{\tau_e, \tau_i, \tau_c, g_{ei}, g_{ii}, \alpha, v\}$ are shown in violin plots. (b) Performance of optimization algorithm. Spectral Pearson's correlation between simulated and MEG spectra at each iteration. Each curve shows the spectral correlation achieved by the model optimized for a single subject. (c) Distribution of spectral correlation between optimized model and observed spectra across subjects. Correlations with optimized parameters and 5 various connectomes are shown in the left-most columns. Correlations with average parameter values and the same connectomes are shown in the middle section. SGM model outperforms an optimized network NMM regardless of connectome type as denoted by asterisk ($p < 0.001$).	40

4.5	Alpha power spatial distribution depicted by specific spectral graph model eigenmodes. (a,b) The spatially distributed patterns of alpha band power for two representative subjects are displayed in brain surface renderings. For each three brain panels shown, the medial surface rendering is shown on the left column while the lateral surface is rendered on the right, the left hemisphere is shown on top and the right hemisphere is shown in the bottom row. Left column: The observed MEG alpha band spatial distribution showing higher power in posterior regions of the brain. Middle column: Spatial distribution of the best matching eigenmode from the SGM. Right column: Spatial distribution of the best cumulative combination of eigenmodes from the SGM. (c) Alpha band spatial correlation for all subjects from SGM simulations with increasing number of cumulative eigenmodes. Individual subject alpha band spatial correlations are shown in cyan ($n = 36$). Panels A and B correspond to the subjects indicated by red and blue curves respectively. Black curve is the average performance across all subjects.	43
4.6	Beta power spatial distribution depicted by specific spectral graph model eigenmodes. Legends and layout is identical to Figure 4.5 but shown for beta band spatial distributions.	44
4.7	Spatial correlation performance of the SGM. Distribution of the SGM for all subjects with the best performing eigenmode. (a) Alpha band spatial correlations. (b) Beta band spatial correlations. For both panels, spatial correlations are shown for SGM with subject individual connectomes (C^{ind} , black), random connectomes with 80% and 95% sparsity (green), geodesic distance based connectome (C^{dist} , blue), and finally for a NMM with specific individual connectome (pink). For each scenario, a selection of the best eigenmodes were obtained for spatial correlation calculations separately. Paired t-tests between SGM(C^{ind}) and all other model simulations show that the SGM with individual connectomes significantly outperform all other models; $p < 0.001$ for all alpha spatial correlations and $p < 0.012$ for all beta spatial correlations.	45

CHAPTER 1

INTRODUCTION

Elucidating how structure shapes observable function is at the heart of a wide spectrum of scientific disciplines. Often, functional units have easily discernible structures governing their roles in a biological system. For example, the 3D molecular structure of a protein forming an ion channel receptor for transport across membranes. As the system becomes more complex, it becomes increasingly difficult to explain emergent function in relation to its underlying structure. Currently, the most complex physical system in the known universe is the central nervous system; the dense synaptic connections and staggering axonal projections in the brains of even simple organisms underly the myriad of fascinating behaviors in nature.

The relationship between the brain's structure and function is of particular interest in neuroscience, as morphological variants of the nervous system have repeatedly been shown to be associated with behavioral changes due to the brain's organizations [1, 2].

A large body of work has beeen devoted to reproducing resting-state brain activity by means of computational modeling

Evidence of correlated activity is observed at the microscopic scale of communicating neurons, prompting extensive efforts to theoretically model these synchronous input and output relationships (sources). While information from single neuron spike recordings can be sufficiently summarized with poisson distributions and probabilistic models (), high dimensional data from whole brain recordings with fMRI, EEG, and MEG require dimensionality reduction for

meaningful interpretation. Graph theory and network theoretics have emerged as an advantagous tool in the field of neuroimaging. By defining specific brain regions of interest (ROIs) as nodes in a network, one can begin dissecting observed functional data

Biophysical models of observable brain data are ... and parameter estimates of such models are a theoretically driven method to reduce the dimensionality of observable brain data for prediction of brain states and clinical statuses [3].

Interpreting model parameter estimates require robust methods to evaluate their generative values, ideally including their uncertainty.

CHAPTER 2

ADVANCES IN DIFFUSION MRI

2.1 Diffusion MRI Processing

Synopsis (¡100 words): Tractography based on diffusion-weighted MRI provides non-invasive *in vivo* estimates of trajectories of long-range brain connections. These estimates are important in research that measures individual differences in brain connections and in clinical use-cases. But the computational demands of tractography present a barrier to progress. Here, we present a GPU-based tractography implementation that accelerates tractography algorithms implemented as part of the Diffusion Imaging in Python (DIPY) project. This implementation speeds up tractography by at least a factor of 200X, providing tractographies that closely match CPU-based solutions. These speedups enable applications of tractography in clinical data, and in very large datasets.

Summary (¡250 characters): GPU-accelerated tractography algorithms that leverage the methods implemented in the DIPY open-source software project accelerate tractography by at least 200-fold, enabling applications to clinical data, as well as very large datasets.

2.2 DESIGNER

2.3 GPU-accelerated Diffusion MRI Tractography in DIPY

2.3.1 Methods

DIPY (Diffusion Imaging in Python; <https://dipy.org>) is an open-source software library that implements many methods in computational neuroanatomy [4]. Relying on the DIPY implementation of residual bootstrap tractography [5], we implemented a multi-GPU parallelizable version constructed on NVIDIA’s CUDA application programming interface (API). The API of the GPU version is compatible with the one implemented in DIPY, enabling direct comparisons and interoperability. A docker container of the software makes the installation and use of the software straightforward. The software is available at <https://github.com/dipy/GPUSstreamlines>. Experiments to profile the performance of the algorithm were conducted using an AWS *p3.16xlarge* instance with 8 NVIDIA Tesla V100 Graphical Processing Units and 488 GB RAM. For comparison, CPU code was run on an AWS *x1e.4xlarge* with 488 GB RAM. We used two datasets, the first is a HARDI acquisition with 2x2x2 mm³ isotropic voxels, 150 b=1,000 s/mm² volumes and 10 b0 volumes previously described in [6]. The other dataset was a Super-Resolution Hybrid Diffusion Imaging (HYDI) dataset [7], with an effective resolution of 0.625 mm³ isotropic voxels, b=500, 800, 1600, 2600 s/mm², in 134 diffusion directions, and 8 b0 volumes, also previously described in [8]. In both cases, 27 seeds were placed in each voxel in the white matter to initialize tracking.

2.3.2 Results

In the HARDI dataset, with the seeding approach used here, approximately 2.1M streamlines were generated. Using the CPU-based residual bootstrap tracking algorithm took approximately 13 hours. The GPU-accelerated implementation provides approximately 200-fold speedup with a single GPU, and up to 671-fold speedup with 8 GPUs run in parallel (Figure 2.1). In the HYDI dataset, the seeding approach used generated 150M streamlines (497GB). Tracking in this case with 8 GPU completed in just under 2 hours. A subset of the HYDI streamlines are shown in Figure 2.2.

2.3.3 Discussion and Conclusion

A GPU-based implementation of residual bootstrap tractography provides orders of magnitude speedup, relative to the CPU-based version, while providing solutions that match CPU-based solutions very closely. This was demonstrated in standard and high-resolution measurements. Thus, this GPU-based implementation allows researchers to both (1) save time and money solving existing problem sizes and (2) solve new problems that are computationally intractable on CPU-only resources. Open-source software is provided, as well as a docker container that encapsulates the software, together with all of its dependencies available at docker.pkg.github.com/dipy/gpustreamlines/gpustreamlines.

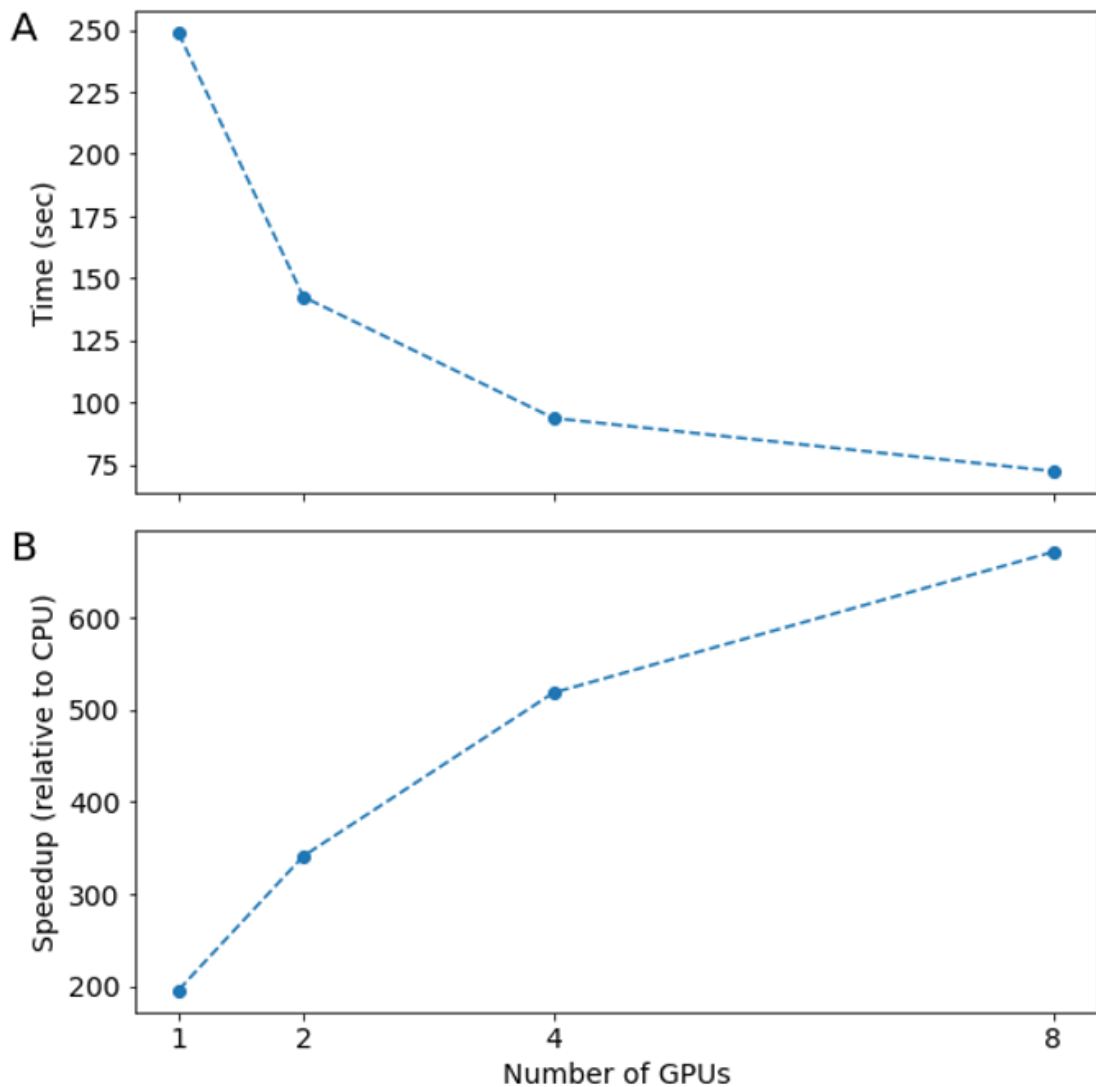


Figure 2.1: For the same task (HARDI data, 27 seeds per WM voxel) tractography duration decreases with the number of GPUs available. Speedup relative to CPU ranges from approximately 200-fold, with one GPU to almost 700-fold with 8 GPUs.

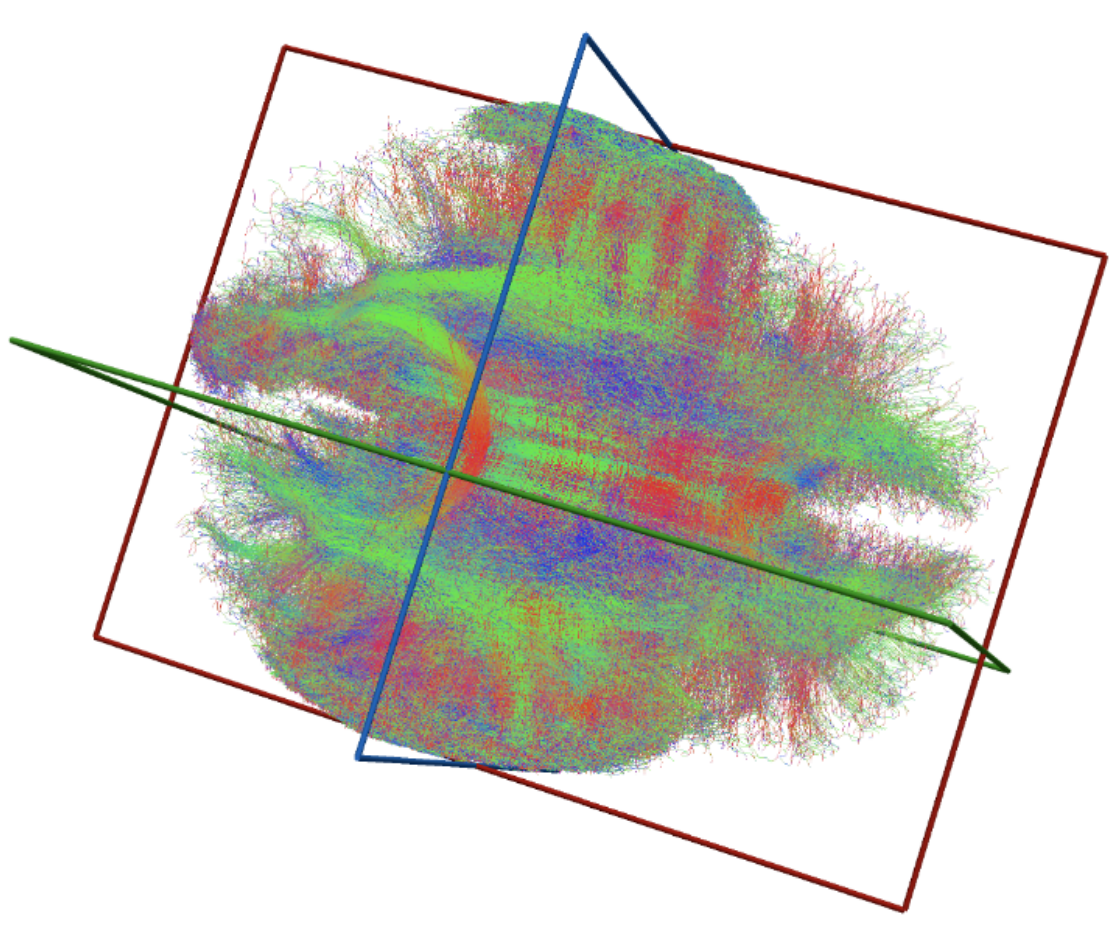


Figure 2.2: GPU-accelerated tractography of high-resolution data, acquired at 0.625 mm^3 effective resolution. This is a small subset sampled randomly for visualization purposes: approximately 8M streamlines of the 150M streamlines tracked.

CHAPTER 3

EMERGENCE OF CANONICAL FUNCTIONAL NETWORKS FROM THE STRUCTURAL CONNECTOME

3.1 Introduction

The exploration of structure and function relationships is a fundamental scientific inquiry at all levels of biological organization, and the structure-function relationship of the brain is of immense interest in neuroscience. Attempts at mathematical formulations of neuronal activity began with describing currents traveling through a neuron's membranes and being charged via ion channels [9]. Recently, the focus of computational models have expanded from small populations of neurons to macroscale brain networks, which are now available via diffusion-weighted and functional magnetic resonance imaging (dMRI and fMRI) [10]. Using computational tractography on dMRI images, detailed whole brain white-matter tracts, and their connectivity can be obtained, to yield the brain's structural connectivity (SC). Using correlated activation patterns over time in fMRI data reveals functional connectivity (FC) with high spatial resolution. Such high resolution images of the brain also allowed neuroscientists to label the brain according to anatomical or functional regions of interest (ROIs) [11, 12]. Subsequently, efforts in graph-theoretic modeling have emerged as an effective computational tool to study the brain's SC-FC relationship based on the parcellated brains: ROIs become nodes and connectivity strengths become edges on the graph, while dynamical systems describing neuronal activity are played out on this graph structure [13, 10, 14].

Diverse graph based methods have been employed to relate the brain's

SC to FC. Particularly, perturbations and evolution of the structural and functional networks have been investigated using both graph theoretical statistics [15, 16, 17, 18, 19, 20, 21] as well as network controllability [22, 23]. Structurally informed models use graphical representations of the brain's connections to couple anatomically connected neuronal assemblies [24, 25], numerical simulations of such neural mass models (NMMs) provides an approximation of the brain's local and global activities, and are able to achieve moderate correlation between simulated and empirical FC [26, 27, 28, 29, 30]. However, approximations through stochastic simulations are unable to provide a closed form solution and inherits interpretational challenges since dynamics is only obtained from iterative optimizations of high dimensional NMM parameters.

An emergent field of work have suggested low-dimensional processes involving diffusion or random walks on the structural graph as a simple means of simulating FC from SC. These simpler models are equally if not more successful at simulating fMRI FC patterns [31, 32] as well as MEG oscillatory patterns [33, 34] than conventional NMMs. Lastly, these simpler graph diffusion models, which naturally employ the Laplacian of SC, have been generalized to yield spectral graph models whereby Laplacian eigen-spectra were sufficient to reproduce functional patterns of brain activity, using only a few eigenmodes [35, 32, 34]. Thus, a Laplacian matrix representation of a network can be used to find characteristic properties of the network [36], and its eigenmodes (or spectral basis) are the ortho-normal basis that represent particular patterns on the network. Such spectral graph models are computationally attractive due to low-dimensionality and more interpretable analytical solutions.

The SC's Laplacian eigenmodes are therefore emerging as the substrate on

which functional patterns of the brain are thought to be established via almost any reasonable process of network transmission [35, 32, 37], and metrics quantifying structural eigenmode coupling strength to functional patterns were also recently introduced [38]. These works mainly focused on replicating canonical functional networks (CFNs), which are stable large scale circuits made up of functionally distinct ROIs distributed across the cortex that were extracted by clustering a large fMRI dataset [39]. In [39] seven CFNs (these are spatial patterns, not to be confused for the entire network of graph of the connectome) were identified. Hence recent graph modeling work has attempted to address whether these canonical patterns can emerge by only looking at the structural connectivity information of the brain.

Although spectral graph models have been reasonably successful, they leave several important gaps. First, they accommodate only passive spread, hence are incapable of producing oscillating or traveling phenomena, which are critical properties of brain functional activity. Second, they do not incorporate path delays caused by finite axonal conductance speed of activity propagating through brain networks. Third, they are capable of reproducing only deterministic and steady-state features of empirical brain activity, giving a single predicted FC for a given SC. Hence these models cannot easily explain the substantial variability observed amongst individuals, as well as between different recording session of the same individual. This suggests that simplistic spectral graph models will need to be augmented with a set of richer time- or individual-varying features or parameters in order to make them more realistic. Unfortunately, this is a goal that is at variance with the key attraction of these methods - their parsimony and low-dimensionality.

In this study we propose a novel spectral graph approach that is able to produce a far richer range of functional activity and dynamics without compromising on the simplicity and parsimony of the spectral graph model. We hypothesise that the introduction of realistic path delays and axonal conductance speeds can allow graph spectra to display the kinds of pattern-richness observed in real data. Hence we utilize both the SC connectivity strength matrix as measured by white-matter fiber tract density, as well as the distance matrix as measured by the average white-matter fiber tract distance between pairs of ROIs. We show that the additional distance information allows for examining of network dynamics in the complex domain in terms of a novel complex-valued Laplacian. This approach involves only global model parameters, which between them accommodate a rich diversity of spatiotemporal patterns that are capable of closely reproducing the diversity of spatial patterning seen across a large number of healthy subjects. Through this minimalist complex diffusion model, the characteristic patterns of signal spread described by corresponding complex-valued eigen-spectra can be tuned to exhibit activation patterns resembling human CFNs. We show that the complex approach significantly and consistently exceeds the performance of existing works relating real-valued SC Laplacian's eigen-spectra to measured FC [32, 38, 35, 29]. The introduction of the complex-valued Laplacian and accompanying complex graph diffusion may be an important contribution to the emerging literature on graph models of brain activity, and furthers our understanding of the structure-function relationship in the human brain.

We begin with a general theory of complex graph diffusion incorporating path delays, leading to the emergence of the complex-valued Laplacian. Then we present detailed statistical analysis showing the ability of complex eigenmodes

to be tuned by model parameters and reproducing CFNs. We present comparison with the current approach of using real-valued eigenmodes, followed by a detailed Discussion.

3.2 Theory

Notation. In our notation, vectors and matrices are represented in **bold**, and scalars by normal font. We denote frequency of a signal, in Hertz (Hz), by symbol f , and the corresponding angular frequency as $\omega = 2\pi f$. The structural connectivity matrix is denoted by $\mathbf{C} = c_{l,m}$, consisting of connection strength $c_{l,m}$ between any two pairs of brain regions l and m .

3.2.1 Network Diffusion of Brain Activity

For an undirected, weighted graph representation of the structural network $c_{l,m}$, we model the average neuronal activation rate for the l -th region as $x_l(t)$:

$$\frac{dx_l(t)}{dt} = -\beta(x_l(t) - \alpha \sum_{l \neq m}^m c_{l,m} x_m(t - \tau_{l,m}^\nu)) + p_l(t) \quad (3.1)$$

Where we have a mean firing rate equation at the m -th region controlled by an inverse of the common characteristic time constant β , and input signals from the l -th regions connected to region m are scaled by the connection strengths from $c_{m,l}$ and delayed by $t - \tau_{m,l}^\nu$. The term $\tau_{m,l}^\nu$ is the delay in seconds obtained from the distance adjacency matrix defined by $\tau_{m,l}^\nu = \frac{D_{m,l}}{\nu}$, with ν representing the conductance speed in the brain's SC network. The global coupling parameter α

acts as a controller of weights given to long-range white-matter connections.

The delays between connected brain regions turn into phase shifts in the frequency profiles of the oscillating signals. Thus we obtain the following Fourier transforms from (3.1): $\frac{dx_l(t)}{dt} \rightarrow j\omega X_l(\omega)$, $x(t - \tau_{m,l}^\nu) \rightarrow e^{-j\omega\tau_{m,l}^\nu} X_m(\omega)$, and the oscillatory frequency $\omega = 2\pi f$. Applying the listed Fourier transforms to (3.1) we can obtain the following:

$$j\omega X_l(\omega) = -\beta(X_l(\omega) - \alpha \sum_{m \neq l} c_{m,l} X_m(\omega) \exp -j\omega\tau_{m,l}^\nu) + p_l(\omega) \quad (3.2)$$

We then define a complex connectivity matrix as a function of angular frequency ω as $\mathbf{C}^*(\omega) = c_{m,l} \exp -j\omega\tau_{m,l}^\nu$. Therefore, a structural connectivity matrix whose nodes are normalized by $\deg_m = \sum_l c_{ml}$ at frequency ω can be expressed as:

$$\mathbf{C}(\omega) = \text{diag}\left(\frac{1}{\deg}\right) \mathbf{C}^*(\omega) \quad (3.3)$$

Replacing the connectivity term in (3.2) with (3.3) and adjusting all vector notations into matrix notation, we derive the following equations for network level activity in the frequency domain:

$$j\omega \mathbf{X}(\omega) = -\beta(\mathbf{X}(\omega) - \alpha \mathbf{X}(\omega) \mathbf{C}(\omega)) + \mathbf{P}(\omega) \quad (3.4)$$

$$\mathbf{X}(\omega)(j\omega \mathbf{I} + \beta(\mathbf{I} - \alpha \mathbf{C}(\omega))) = \mathbf{P}(\omega) \quad (3.5)$$

3.2.2 Complex Laplacian Matrix

Our goal is to examine the characteristic patterns of diffusion revealed by the structural network's normalized Laplacian matrix. Here, we make use of (3.3) to introduce a complex Laplacian matrix that absorbs the network properties of both the structural connectivity matrix as well as the distance adjacency matrix. By substituting the complex Laplacian matrix and rebalancing (3.5), we obtain a closed-form solution for $\tilde{\mathbf{X}}(\omega)$:

$$\mathbf{X}(\omega) = (j\omega I + \beta \mathcal{L}(\alpha, k))^{-1} \mathbf{P}(\omega) \quad (3.6)$$

In this closed-form solution, we defined a complex Laplacian matrix \mathcal{L} as a function of global coupling strength α and wave number k , which facilitates the dynamics and frequency profiles observed on the brain's connectome. Since frequency ω and transmission speed v always occur as a ratio, we define the wave number $k = \frac{\omega}{v}$. The wave number represents the spatial frequency of any propagating wave, describing the amount of oscillations per unit distance traveled [40]. Then the complex Laplacian matrix \mathcal{L} has the form:

$$\mathcal{L}(\alpha, k) = \mathbf{I} - \alpha \mathbf{C}^*(k) \quad (3.7)$$

Where \mathbf{I} is the identity matrix and $\mathbf{C}^*(k)$ is the complex connectivity matrix as defined above. While (3.3) indicates that the propagating signals in the network is governed by \mathcal{L} , the complex Laplacian of the network describes the characteristic patterns of signal spread in a network, and we can obtain these spatial patterns via the decomposition:

$$\mathcal{L}(\alpha, k) = \sum_{n=1}^N \mathbf{u}_n(\alpha, k) \lambda_n(\alpha, k) \mathbf{u}_n^H(\alpha, k) \quad (3.8)$$

Where $\lambda_n(\alpha, k)$ are the eigenvalues of the complex Laplacian matrix and $\mathbf{u}_n(\alpha, k)$'s are the complex eigenmodes of the complex Laplacian matrix. Here, the entries of the complex Laplace eigenmodes represent the relative amount of activation in each parcellated brain region as controlled by global coupling and wave number parameters.

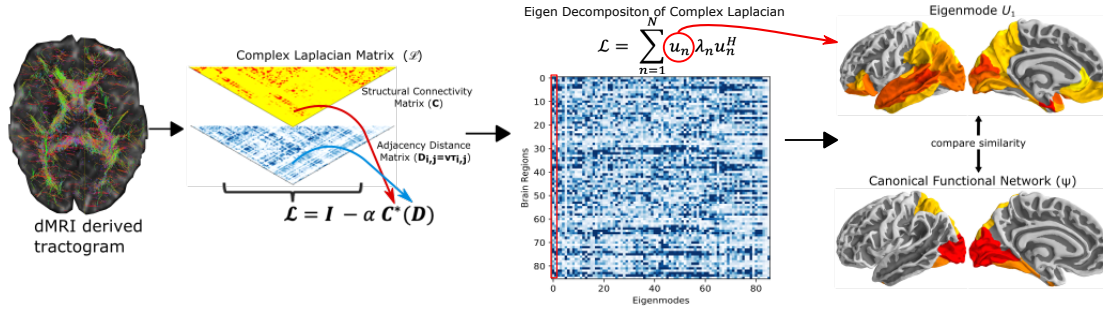


Figure 3.1: The analysis overview. Structural connectivity matrix (C) and distance adjacency matrix (D) were extracted from diffusion MRI derived tractograms, to construct the complex Laplacian of the brain's structural network. An eigen decomposition on the network's complex Laplacian (\mathcal{L}) was performed obtain complex structural eigenmodes of the brain (U). The spatial similarities were computed between the structural eigenmodes and canonical functional networks in fMRI. Here, as an example, we show brain rendering of the leading eigenmode from the HCP template structural connectome (right column, top) and the canonical visual functional network (right column, bottom).

CHAPTER 4

SPECTRAL GRAPH THEORY OF BRAIN OSCILLATIONS

4.1 Introduction

4.1.1 The Structure-Function Problem in Neuroscience

It is considered paradigmatic in neuroscience that the brain's structure at various spatial scales is critical for determining its function. In particular, the relationship between the brain's *structural wiring* and the *functional* patterns of neural activity is of fundamental interest in computational neuroscience. Brain structure and function at the scale of macroscopic networks, i.e. amongst identifiable grey matter (GM) regions and their long-range connections through white matter (WM) fiber bundles, can be adequately measured using current non-invasive measurement techniques. Fiber architecture can be measured from diffusion tensor imaging (DTI) followed by tractography algorithms [41, 42]. Similarly, brain function manifested in neural oscillations can be measured non-invasively using magnetoencephalography (MEG) and reconstructed across whole-brain networks. Does the brain's white matter wiring structure constrain functional activity patterns that arise on the macroscopic network or graph, whose nodes represent gray matter regions, and whose edges have weights given by the structural connectivity (SC) of white matter fibers between them? We address this critical open problem here, as the structural and functional networks estimated at various scales are not trivially predictable from each other [29].

Although numerical models of single neurons and local microscopic neuronal

assemblies, ranging from simple integrate-and-fire neurons to detailed multi-compartment and multi-channel models [43, 44, 45, 46, 47] have been proposed, it is unclear if these models can explain structure-function coupling at meso- or macroscopic scales. At one extreme, the Blue Brain Project [48, 49] seeks to model in detail all 10^{11} neurons and all their connections in the brain. Indeed spiking models linked up via specified synaptic connectivity and spike timing dependent plasticity rules were found to produce regionally and spectrally organized self-sustaining dynamics, as well as wave-like propagation similar to real fMRI data [50]. However, it is unclear whether such efforts will succeed in providing interpretable models at whole-brain scale [51].

Therefore the traditional computational neuroscience paradigm at the microscopic scale does not easily extend to whole-brain macroscopic phenomena, as large neuronal ensembles exhibit emergent properties that can be unrelated to individual neuronal behavior [52, 53, 54, 55, 56, 31], and are instead largely governed by long-range connectivity [57, 58, 59, 60]. At this scale, graph theory involving network statistics can phenomenologically capture structure-function relationships [61, 10, 62], but do not explicitly embody any details about neural physiology [53, 54]. Strong correlations between functional and structural connections have also been observed at this scale [29, 31, 63, 64, 65, 66, 35, 67], and important graph properties are shared by both SC and functional connectivity (FC) networks, such as small worldness, power-law degree distribution, hierarchy, modularity, and highly connected hubs [10, 68].

A more detailed accounting of the structure-function relationship requires that we move beyond statistical descriptions to mathematical ones, informed by computational models of neural activity. Numerical simulations are available of

mean field [56, 25, 69] and neural mass [60, 70] approximations of the dynamics of neuronal assemblies. By coupling many such neural field or mass models (NMMs) using anatomic connectivity information, it is possible to generate via large-scale stochastic simulations a rough picture of how the network modulates local activity at the global scale to allow the emergence of coherent functional networks [60]. However, simulations are unable to give an analytical (i.e. closed form) encapsulation of brain dynamics and present an interpretational challenge in that behavior is only deducible indirectly from thousands of trial runs of time-consuming simulations. Consequently, the essential minimal rules of organization and dynamics of the brain remain unknown. Furthermore, due to their nonlinear and stochastic nature, model parameter inference is ill-posed, computationally demanding and manifest with inherent identifiability issues (cite identifiability paper here).

How then do stereotyped spatiotemporal patterns emerge from the structural substrate of the brain? How will disease processes perturb brain structure, thereby impacting its function? While stochastic simulations are powerful and useful tools, they provide limited neuroscientific insight, interpretability and predictive power, especially for the practical task of inferring macroscopic functional connectivity from long-range anatomic connectivity. Therefore, there is a need for more direct models of structural network-induced neural activity patterns – a task for which existing numerical modeling approaches, whether for single neurons, local assemblies, coupled neural masses or graph theory, are not ideally suited. Here we use a spectral graph model (SGM) to demonstrate that the spatial distribution of certain brain oscillations are emergent properties of the spectral graph structure of the structural connectome. Therefore, we also explore how the chosen connectome alters the functional activity patterns they sustain.

4.1.2 A hierarchical, analytic, low-dimensional and linear spectral graph theoretic model of brain oscillations

We present a linear graph model capable of reproducing empirical macroscopic spatial and spectral properties of neural activity. We are interested specifically in the transfer function (defined as the frequency-domain input-output relationship) induced by the macroscopic structural connectome, rather than in the behavior of local neural masses. Therefore we seek an explicit formulation of the frequency spectra induced by the graph, using the eigen-decomposition of the structural graph Laplacian, borrowing heavily from **spectral graph theory** used in diverse contexts including clustering, classification, and machine learning [71, 72, 73, 74]. This theory conceptualizes brain oscillations as a linear superposition of eigenmodes. These eigen-relationships arise naturally from a biophysical abstraction of fine-scaled and complex brain activity into a simple linear model of how mutual dynamic influences or perturbations can spread within the underlying structural brain network, a notion that was advocated previously [31, 75, 76]. We had previously reported that the brain network Laplacian can be decomposed into its constituent "eigenmodes", which play an important role in both healthy brain function [31, 35, 77, 32] and pathophysiology of disease [77, 78, 79, 80].

We show here that a graph-spectral decomposition is possible at all frequencies, ignoring non-linearities that are operating at the local (node) level. Like previous NMMs, we lump neural populations at each brain region into neural masses, but unlike them we use a linearized (but frequency-rich) local model – see **Figure 1A**. The macroscopic connectome imposes a linear and deterministic modulation of these local signals, which can be captured by a *network transfer function*. The sequestration of local oscillatory dynamics from the macroscopic

network in this way enables the characterization of whole brain dynamics deterministically in closed form in Fourier domain, via the eigen-basis expansion of the network Laplacian. As far as we know, this is the first closed-form analytical model of frequency-rich brain activity constrained by the structural connectome.

We applied this model to and validated its construct against measured source-reconstructed MEG recordings in healthy subjects under rest and eyes-closed. The model closely matches empirical spatial and spectral MEG patterns. In particular, the model displays prominent alpha and beta peaks, and, intriguingly, the eigenmodes corresponding to the alpha oscillations have the same posterior-dominant spatial distribution that is repeatedly seen in eyes-closed alpha power distributions. In contrast to existing less parsimonious models in the literature that invoke spatially-varying parameters or local rhythm generators, to our knowledge, this is the first account of how the spectral graph structure of the structural connectome can parsimoniously explain the spatial power distribution of alpha and beta frequencies over the entire brain measurable on MEG.

4.2 Methods

4.2.1 Spectral graph model development

Notation. In our notation, vectors and matrices are represented by boldface, and scalars by normal font. We denote frequency of a signal, in Hertz, by symbol f , and the corresponding angular frequency as ($\omega = 2\pi f$). The connectivity matrix is denoted by $\mathbf{C} = \{c_{jk}\}$, consisting of connectivity strength c_{ij} between any two pair of regions j, k .

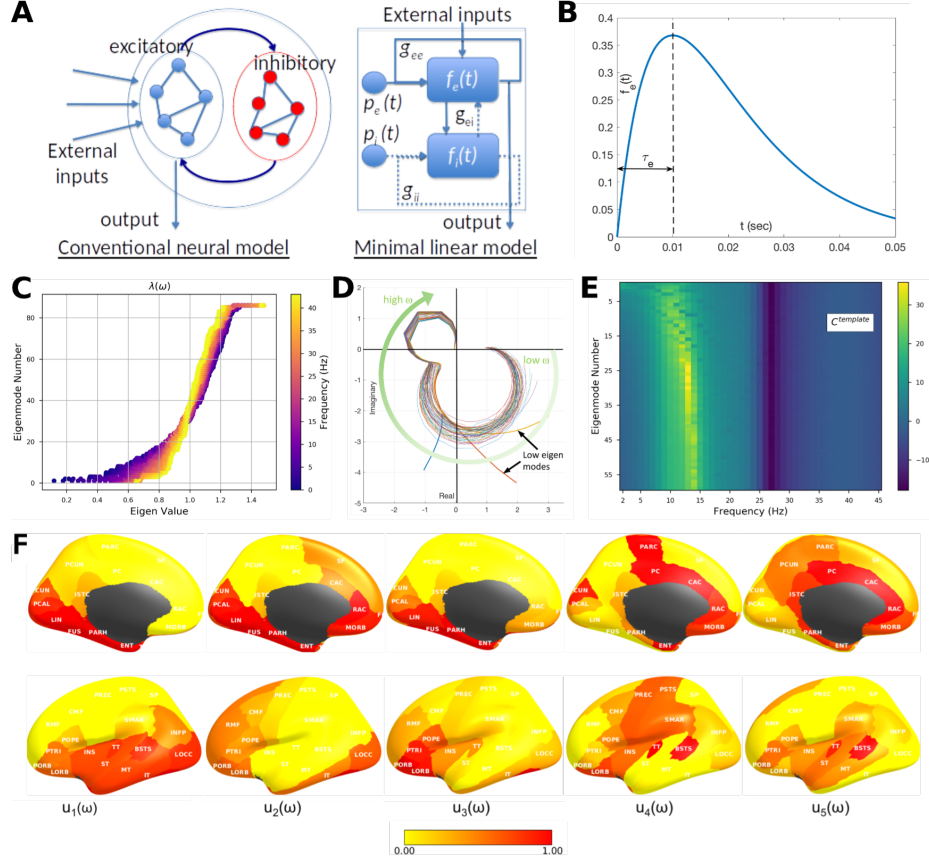


Figure 4.1: The linearized spectral graph model. (a) Conventional neural mass models instantiate a large assembly of excitatory and inhibitory neurons, which are modeled as fully connected internally. External inputs and outputs are gated through the excitatory neurons only, and inhibitory neurons are considered strictly local. The proposed linear model condenses these local assemblies into lumped linear systems $f_e(t)$ and $f_i(t)$, Gamma-shaped functions having time constants τ_e and τ_i (see panel (b)). The recurrent architecture of the two pools within a local area is captured by the gain terms g_{ee} , g_{ii} , g_{ei} , parameterizing the recurrences within excitatory, inhibitory and cross-populations. (c) The absolute value of eigenvalues of the complex Laplacian $\mathcal{L}(\omega)$ are plotted against the eigenvector index. Each dot represents one eigenvalue $\lambda(\omega)$; its color represents the frequency ω - low (blue) to high (yellow). These eigenvalues change by frequency; small eigenvalues change more compared to large ones. (d) Frequency response of each eigenmode plotted on the complex plane with default model parameters and a template structural connectome. Each curve represents the transit in the complex plane of a single eigenmode's frequency response, starting at low frequencies in the bottom right quadrant, and moving to the upper left quadrant at high frequencies. The magnitude of the response, given by the distance from the origin, suggests that most eigenmodes have two prominent lobes, roughly corresponding to lower frequency alpha rhythms and higher frequency gamma rhythms. In contrast, the lowest eigenmodes start off far from the origin, indicative of a low-pass response. (e) Magnitude of the frequency response of each eigenmode reinforces these impressions more clearly, with clear alpha peak, as well as slower rhythms. (f) The spatial patterns of the top 5 eigenmodes of $\mathcal{L}(\omega)$, evaluated at the alpha frequency. The first 5 eigenmodes $u_1 \dots u_5$ produce resting-state functional networks patterns; These patterns are not exclusive and greatly depend on the frequency, model parameters, and the connectome.

Table 4.1: SGM parameters values and limits

Name	Symbol	Default Value	Optimizaiton Bounds
Excitatory Time constant	τ_e	12 ms	[5ms, 20ms]
Inhibitory Time constant	τ_i	3 ms	[5ms, 20ms]
Graph Time constant	τ_G	6 ms	[5ms, 20ms]
Excitatory gain	g_{ee}	1	n/a
Inhibitory gain	g_{ii}	1	[0.5, 5]
Excitatory gain	g_{ei}	4	[0.5, 5]
Transmission velocity	v	5 m/s	[5 m/s, 20 m/s]
Long-range connectivity coupling constant	α	1	[0.1, 1]

Model summary: Details of the Spectral Graph model (SGM) is described in detail below. There are very few model parameters, seven in total: $\tau_e, \tau_i, \tau_G, v, g_{ii}, g_{ei}, \alpha$, which are all global and apply at every node. See Table 4.1 for their meaning, initial value and range. Note that the entire model is based on a single equation of graph dynamics, Eq 4.1, which is repeatedly applied to each level of the hierarchy. Here we used two levels: a mesoscopic level where connectivity is all-to-all, and a macroscopic level, where connectivity is measured from fiber architecture. In theory, this template could be refined into finer levels, where neural responses become increasingly non-linear, and connectivity becomes sparser and structured.

Canonical rate model over a graph. We use a canonical rate model to describe neural activity across two hierarchical levels – local cortical mesoscopic levels and long-range macroscopic levels. At each level of the hierarchy of brain circuits, we hypothesize a simple linear rate model of recurrent reverberatory activity given by

$$\frac{dx_{e/i}(t)}{dt} = -\frac{1}{\tau_{e/i}} f_{e/i}(t) * x_{e/i}(t) + \frac{1}{\tau_{e/i}} f_{e/i}(t) * \sum_{j,k} c_{jk} x_{e/i}(t - \tau_{jk}^v) + p_{e/i}(t) \quad (4.1)$$

where $x_{e/i}(t)$ is the mean signal of the excitatory/inhibitory populations and $p_{e/i}(t)$ is internal noise source reflecting local cortical column computations or input. The transit of signals, from pre-synaptic membranes, through dendritic arbors and axonal projections, is sought to be captured into ensemble average neural impulse response functions $f_e(t) = \frac{t}{\tau_e} \exp(-\frac{t}{\tau_e})$ and $f_i(t) = \frac{t}{\tau_i} \exp(-\frac{t}{\tau_i})$ respectively. We disregard the non-linearity of the neural response, hence the output at the terminal to a presynaptic input $u(t)$ is the simple convolution $x_e(t) = f_e(t) * u(t)$. The neural responses $f_{e/i}(t)$ are Gamma-shaped responses (Figure 4.1B) parameterized by time constants $\tau_{e/i}$ that here represent the end result of both synaptic membrane capacitance and the distribution of dendritic/axonal delays introduced by the arborization. NMMs typically use a single classical exponential decay term for membrane capacitance only, since NMMs model highly local cell assemblies where multisynaptic connections are infrequent and axonal and dendritic transport delays are usually incorporated explicitly via connectivity weights and delays. Since our lumped model was designed for relatively large cortical regions, we employ the Gamma-shaped $f_{e/i}$ to capture not just classical membrane capacitance but also the expected diversity of dendritic transport delays. The dynamics of the entire assembly modeled via a self-decaying term $\tau_{e/i} \frac{d\mathbf{x}}{dt} \propto -f_{e/i}(t) * \mathbf{x}(t)$, typically used in most rate or NMM models, but the difference here is that we chose to apply convolution with neural response $f_{e/i}(t)$ within the decay process. We believe this is necessary to ensure that the dynamics of the population cannot participate in the internal recurrent dynamics of the region until the signal has passed through one instance of the neuronal response. Since

this neural response is meant to capture a distribution of local circuit delays, its time constants $\tau_{e/i}$ are purposefully far longer (up to 20ms) than expected from membrane capacitance alone. Studies of cortical lag times using paired electrode recordings between primary and higher cortices demonstrate this. A short visual stimulus causes a neural response in the ferret V1 within 20ms post-stimulus, in the primary barrel field within 16-36ms, and the entire visual cortex becomes engaged 48-70ms after stimulus [45]. Brief deflection of a single barrel whisker in the mouse evokes a somatotopically mapped cortical depolarization that remains localized to its C2 barrel column only for a few milliseconds, thence rapidly spreading to a large part of sensorimotor cortex within tens of milliseconds, a mechanism considered essential for the integration of sensory information [81, 82]. Interestingly, the evoked response curve in S1 from the ⁵⁰ study had a prominent Gamma shape. Of note, the duration of S1 response (\sim 50ms) was considerably longer than the time to first sensory response in C2 (7.2ms) [81]. Interestingly, feedback projections from higher to lower areas take \sim 50ms, hence have a much slower apparent propagation velocity (0.15-0.25m/s) than what would be predicted by axonal conduction alone (1-3m/s) [45].

Individual neural elements are connected to each other via connection strengths c_{jk} . Let the cortico-cortical fiber conduction speed be v , which here is assumed to be a global constant independent of the pathway under question. For a given pathway connecting regions j and k of length d_{jk} , the conduction delay of a signal propagating from region j to region k will be given by $\tau_{jk}^v = \frac{d_{jk}}{v}$. Hence signals from neighboring elements also participate in the same recurrent dynamics, giving the second term of Eq 4.1. Equation 4.1 will serve as our canonical rate model, and will be reproduced at all levels of the hierarchy, and only the connectivity strengths will vary depending on the level of hierarchy we are

modeling, as explained below.

Local neural assemblies. The local connectivities c_{jk}^{local} are assumed to be all-to-all, giving a complete graph. Further, the axonal delays τ_{jk}^v associated with purely local connections were already incorporated in the lumped impulse responses $f_{e/i}(t)$. Hence, we assert:

$$c_{jk}^{local} = c_{e/i}, \quad \tau_{jk}^v = 0, \quad \forall j, k \quad (4.2)$$

From spectral graph theory, a complete graph has all equal eigenvalues which allows the local network to be lumped into gain constants, and the summation removed. Indeed, rewriting $x_{e/i}(t)$ as the mean signal of all the excitatory/inhibitory cells and setting the gains $g_{ee} = 1 - c_e N_e$ and $g_{ii} = 1 - c_i N_i$ we get

$$\frac{dx_{e/i}(t)}{dt} = -\frac{g_{ee/ii}}{\tau_{e/i}} f_{e/i}(t) * x_{e/i}(t) + p_{e/i}(t) \quad (4.3)$$

Given the Fourier Transform pairs $\frac{d}{dt} \leftrightarrow j\omega$, $f_{e/i}(t) \leftrightarrow F_{e/i}(\omega) = \frac{1/\tau_{e/i}^2}{(j\omega + 1/\tau_{e/i})^2}$, we take the Fourier transform of Eq 4.1 and obtain the local assembly's frequency spectrum:

$$X_{e/i}(\omega) = (j\omega + \frac{g_{ee/ii}}{\tau_{e/i}} F_{e/i}(\omega))^{-1} P_{e/i}(\omega) \quad (4.4)$$

Writing this in terms of transfer functions $X_e(\omega) = H_e(\omega)P_e(\omega)$, $X_i(\omega) = H_i(\omega)P_i(\omega)$ we get the lumped local system illustrated in Figure 4.1. Finally, we must also account for signals that alternate between the two populations, which is given by the transfer function

$$H_{ei}(\omega) = H_e(\omega)H_i(\omega)/(1 + g_{ei}H_e(\omega)H_i(\omega)) \quad (4.5)$$

We fix $g_{ee} = 1$ without loss of generality, and let the other terms g_{ii}, g_{ei} be model parameters to be fitted. Finally, the total cortical transfer function is the sum

$$H_{local}(\omega) = H_e(\omega) + H_i(\omega) + H_{ei}(\omega) \quad (4.6)$$

and $X_{local}(\omega) = H_{local}(\omega)P(\omega)$ represents all neural activity in this region, whether from excitatory or inhibitory cells. The canonical local activity is therefore defined by the Fourier transform pair: $x_{local}(t) \leftrightarrow X_{local}(\omega)$.

4.2.2 Macroscopic scale: signal evolution on the entire graph

For the macroscopic level, we use the same canonical network dynamics as Eq 4.1, but now the inter-regional connectivity c_{jk} is non-zero and given by the structural connectome. Similarly, axonal conductance delays are determined by fiber length and conductance speed $\tau_{jk}^v = d_{jk}/v$. Further, the external driving signals at each node is the local neural activity $x_{local}(t)$ defined above rather than a noise process $p(t)$. In the interest of parsimony we set each node of the macroscopic graph to have the same internal power spectrum $X_{local}(\omega)$ - i.e. all regions are experiencing the same transfer function, driven by identically distributed (but of course not identical) noise. At this scale, activity measured at graph nodes is no longer excitatory or inhibitory, but mixed, and the corticocortical connections are all between long, pyramidal excitatory-only cells. Thus, for the k-th node

$$\frac{dx_k(t)}{dt} = -\frac{1}{\tau_G} f_e(t) * x_k(t) + \frac{\alpha}{\tau_G} f_e(t) * \sum_j c_{jk} x_j(t - \tau_{jk}^v) + x_{local,k}(t) \quad (4.7)$$

Here we have introduced a global coupling constant α , similar to most connectivity-coupled neural mass models, that seeks to control the relative weight given to long-range afferents compared to local signals. We have also introduced a new time constant, τ_G , which is an excitatory time constant and it may be the same as the previously used constant τ_e . However, we allow the possibility that the long-range projection neurons might display a different capacitance and morphology compared to local circuits, hence we have introduced τ_G (subscript G is for “graph” or “global”).

Stacking all equations from all nodes and using vector valued signals $\mathbf{x}(t) = x_k(t)$, we can write

$$\frac{d\mathbf{x}(t)}{dt} = -\frac{1}{\tau_G} f_e(t) * \mathbf{x}(t) + \frac{\alpha}{\tau_G} f_e(t) * C\{\mathbf{x}(t - \tau_{jk}^v)\} + \mathbf{x}_{local}(t) \quad (4.8)$$

where the braces $\{\cdot\}$ represent all elements of a matrix indexed by j, k .

We wish to evaluate the frequency spectrum of the above. In Fourier space, delays become phases; hence we use the transform pairs $\frac{dx}{dt} \leftrightarrow j\omega \mathbf{X}(\omega)$ and $\mathbf{x}(t - \tau) \leftrightarrow e^{-j\tau\omega} \mathbf{X}(\omega)$. Therefore, define a “complex connectivity matrix” at any given angular frequency ω as $\mathbf{C}^*(\omega) = c_{jk} \exp(-j\omega\tau_{jk}^v)$. We then define a normalized complex connectivity matrix at frequency ω as

$$C(\omega) = \text{diag}\left(\frac{1}{\deg}\right) \mathbf{C}^*(\omega) \quad (4.9)$$

where the degree vector deg is defined as $\text{deg}_k = \sum_j c_{jk}$. Taking the Fourier transform of Equation 4.8, we get

$$(j\omega \mathbf{X}(\omega) + \frac{1}{\tau_G} F_e(\omega)(\mathbf{I} - \alpha C(\omega))\mathbf{X}(\omega)) = H_{local}(\omega)\mathbf{P}(\omega) \quad (4.10)$$

where we assumed identically distributed noise signals driving both the excitatory and inhibitory local populations at each node, such that $P_{e,k}(\omega) = P_{i,k}(\omega) = P_k(\omega)$ at the k -th node. We then collected all nodes' driving inputs in the vector $\mathbf{P}(\omega) = P_k(\omega), \forall k$. Here, we define the complex Laplacian matrix

$$\mathcal{L}(\omega) = \mathbf{I} - \alpha C(\omega) \quad (4.11)$$

where \mathbf{I} is the identity matrix of size $N \times N$. This complex Laplacian will be evaluated via the eigen-decomposition

$$\mathcal{L}(\omega) = \mathbf{U}(\omega)\Lambda(\omega)\mathbf{U}(\omega)^H \quad (4.12)$$

where $\Lambda(\omega) = \text{diag}([\lambda_1(\omega), \dots, \lambda_N(\omega)])$ is a diagonal matrix consisting of the eigenvalues of the complex Laplacian matrix of the connectivity graph $C(\omega)$, at the angular frequency ω .

Hence

$$\mathbf{X}(\omega) = (j\omega \mathbf{I} + \frac{1}{\tau_G} F_e(\omega)\mathcal{L}(\omega))^{-1} H_{local}(\omega)\mathbf{P}(\omega) \quad (4.13)$$

where we invoke the eigen-decomposition of $\mathcal{L}(\omega)$, and that $\mathbf{U}(\omega)\mathbf{U}(\omega)^H = \mathbf{I}$. It can then be shown easily that

$$\mathbf{X}(\omega) = \sum_i \frac{\mathbf{u}_i(\omega)\mathbf{u}_i^H(\omega)}{j\omega + \frac{1}{\tau_G}\lambda_i(\omega)F_e(\omega)} H_{local}(\omega)\mathbf{P}(\omega) \quad (4.14)$$

This is the steady state frequency response of the whole brain dynamics. In steady state, we assume that each cortical region is driven by internal noise that spans all frequencies, i.e. white noise. Hence, we assume that the driving function $\mathbf{p}(t)$ is an uncorrelated Gaussian noise process, such that $\mathbf{P}(\omega) = \mathbb{I}$ where \mathbb{I} is a vector of ones. This asserts identical cortical responses at each brain region.

4.2.3 Experimental Procedures

Study cohort. We acquired MEG, anatomical MRI, and diffusion MRI for 36 healthy adult subjects (23 males, 13 females; 26 left-handed, 10 right-handed; mean age 21.75 years (range: 7-51 years). All study procedures were approved by the institutional review board at the University of California at San Francisco (UCSF) and are in accordance with the ethics standards of the Helsinki Declaration of 1975 as revised in 2008.

MRI. A 3 Tesla TIM Trio MR scanner (Siemens, Erlangen, Germany) was used to perform MRI using a 32-channel phased-array radiofrequency head coil. High-resolution MRI of each subject's brain was collected using an axial 3D magnetization prepared rapid-acquisition gradient-echo (MPRAGE) T1-weighted sequence (echo time [TE] = 1.64 ms, repetition time [TR] = 2530 ms, TI = 1200 ms, flip angle of 7 degrees) with a 256-mm field of view (FOV), and 160 1.0-mm contiguous partitions at a 256×256 matrix. Whole-brain diffusion weighted images were collected at $b = 1000 s/mm^2$ with 30 directions using 2-mm voxel resolution in-plane and through-plane.

Magneto-encephalography (MEG) data. MEG recordings were acquired at UCSF using a 275-channel CTF Omega 2000 whole-head MEG system from VSM MedTech (Coquitlam, BC, Canada). All subjects were instructed to keep their eyes closed for five minutes while their MEGs were recorded at a sampling frequency of 1200 Hz.

4.2.4 Data Processing

Region Parcellations. The T1-weighted images were parcellated into 68 cortical regions and 18 subcortical regions using the Desikan-Killiany atlas available in the FreeSurfer software [83]. To do this, the subject specific T1-weighted images were back-projected to the atlas using affine registration, as described in our previous studies [31, 84].

Structural Connectivity Networks. We constructed different structural connectivity networks with the same Desikan-Killiany parcellations to access the capabilities of our proposed model. Firstly, we obtained openly available diffusion MRI data from the MGH-USC Human Connectome Project to create an average template connectome. As in our previous studies [31, 84], subject specific structural connectivity was computed on diffusion MRI data: *Bedpostx* was used to determine the orientation of brain fibers in conjunction with *FLIRT*, as implemented in the *FSL* software [85]. In order to determine the elements of the adjacency matrix, we performed tractography using *probtrackx2*. We initiated 4000 streamlines from each seed voxel corresponding to a cortical or subcortical gray matter structure and tracked how many of these streamlines reached a target gray matter structure. The weighted connection between the two structures

$c_{i,j}$, was defined as the number of streamlines initiated by voxels in region i that reach any voxel within region j , normalized by the sum of the source and target region volumes ($c_{i,j} = \frac{\text{streamlines}}{v_i + v_j}$). This normalization prevents large brain regions from having high connectivity simply due to having initiated or received many streamlines. Afterwards, connection strengths are averaged between both directions ($c_{i,j}$ and $c_{j,i}$) to form undirected edges. It is common in neuroimaging literature to threshold connectivity to remove weakly connected edges, as this can greatly influence the implied topology of the graph. In our work, we chose not to apply further thresholding, as unlike conventional graph theoretic metrics, linear models of spread and consequently network eigenmodes are relatively insensitive to implied topology induced by presence (or lack) of weak nonzero connections. However, to determine the geographic location of an edge, the top 95% of non-zero voxels by streamline count were computed for both edge directions. The consensus edge was defined as the union between both post-threshold sets.

MEG processing and source reconstruction. MEG recordings were down-sampled from 1200 Hz to 600 Hz, then digitally filtered to remove DC offset and any other noisy artifact outside of the 1 to 160 Hz bandpass range. Since MEG data are in sensor space, meaning they represent the signal observable from sensors placed outside the head, this data needs to be “inverted” in order to infer the neuronal activity that has generated the observed signal by solving the so-called inverse problem. Several effective methods exist for performing *source localization* [86, 87, 88]. Here we eschew the common technique of solving for a small number of discrete dipole sources which is not fully appropriate in the context of inferring resting state activity, since the latter is neither spatially sparse nor localized. Instead, we used adaptive spatial filtering algorithms from

the NUTMEG software tool written in house [89] in MATLAB (The MathWorks, Inc., Natick, Massachusetts, United States). To prepare for source localization, all MEG sensor locations were co-registered to each subject's anatomical MRI scans. The lead field (forward model) for each subject was calculated in NUTMEG using a multiple local-spheres head model (three-orientation lead field) and an 8 mm voxel grid which generated more than 5000 dipole sources, all sources were normalized to have a norm of 1. Finally, the MEG recordings were projected into source space using a beamformer spatial filter. Source estimates tend to have a bias towards superficial currents and the estimates are more error-prone when we approach subcortical regions, therefore, only the sources belonging to the 68 cortical regions were selected to be averaged around the centroid. Specifically, all dipole sources were labeled based on the Desikan-Killiany parcellations, then sources within a 20 mm radial distance to the centroid of each brain region were extracted, the average time course of each region's extracted sources served as empirical resting-state data for our proposed model.

Alternative benchmark model for comparison. In order to put the proposed model in context, we also implemented for comparison a Wilson-Cowan neural mass model [56, 69, 23] (add criticism citation here) with similar dimensionality. Although NMMs like this can and have been implemented with regionally varying local parameters, here we enforced uniform, regionally non-varying local parameters, meaning all parcellated brain regions shared the same local and global parameters. This is a fair comparison since the proposed model is also regionally non-varying. The purpose of this exercise is to ascertain whether a non-regional NMM can also predict spatial power variations purely as a consequence of network transmission, like the proposed model, using the same model optimization procedure (see below). This NMM incorporates a transmission

velocity parameter that introduces a delay based on fiber tract lengths extracted from diffusion MRI, but, unlike our model, does not seek to explicitly evaluate a frequency response based on these delays.

4.2.5 Model Optimization

We computed *maximum a posteriori* estimates for parameters under a flat non-informative prior. A simulated annealing optimization algorithm was used for estimation and provided a set of optimized parameters $\{\tau_e, \tau_i, \tau_c, g_{ei}, g_{ii}, \alpha, v\}$. We defined a data likelihood or goodness of fit (GOF) as the Pearson correlation between empirical source localized MEG power spectra and simulated model power spectra, averaged over all 68 regions of a subject's brain. The proposed model has only seven global parameters as compared to neural mass models with hundreds of parameters, and is available in closed-form. To improve the odds that we capture the global minimum, we chose to implement a probabilistic approach of simulated annealing [90]. The algorithm samples a set of parameters within a set of boundaries by generating an initial trial solution and choosing the next solution from the current point by a probability distribution with a scale depending on the current "temperature" parameter. While the algorithm always accepts new trial points that map to cost-function values lower than the previous cost-function evaluations, it will also accept solutions that have cost-function evaluations greater than the previous one to move out of local minima. The acceptance probability function is $1/(1 + \frac{\Delta}{e^{\max(T)}})$, where T is the current temperature and Δ is the difference of the new minus old cost-function evaluations. The initial parameter values and boundary constraints for each parameter are given in Table 4.1. All simulated annealing runs were allowed to

iterate over the parameter space for a maximum of $N_p \times 3000$ iterations, where N_p is the number of parameters in the model. As a comparison, we performed the same optimization procedure to a regionally non-varying Wilson-Cowan neural mass model [69, 23].

4.3 Results

4.3.1 Graph Laplacian eigenmodes mediate a diversity of frequency responses

First, we demonstrate the spectra produced by graph eigenmodes as per our theory using default choices of model parameters. Figure 4.1C shows the eigen-spectrum of the complex Laplacian, with eigenvalue magnitude ranging from 0 to 1. The absolute value of eigenvalues of the complex Laplacian $\mathcal{L}(\omega)$ are plotted against the eigenvector index. Each dot represents one eigenvalue $\lambda(\omega)$; its color represents the frequency ω - low (blue) to high (yellow). Clearly, these eigenvalues change somewhat by frequency. Small eigenvalues undergo a larger shift due to frequency, while the large ones stay more stable and tightly clustered around the nominal eigenvalue (i.e. at $\omega = 0$). Each eigenmode produces a frequency response based on its frequency-dependent eigenvalue (Figure 4.1D, E). Figure 4.1D shows the transit in the complex plane of a single eigenmode's frequency response, starting at low frequencies in the bottom right quadrant, and moving to the upper left quadrant at high frequencies. The magnitude, given by distance from origin, suggests that most eigenmodes have two prominent lobes, one roughly corresponding to lower frequency alpha rhythm and another

corresponding to higher frequency beta or gamma rhythms, respectively. In contrast, the lowest few eigenmodes start off far from the origin, indicative of a low-pass response. The magnitude of these complex-valued curves shown in Figure 4.1E reinforces these impressions, with clear alpha peak, as well as slower rhythms of the lowest eigenmodes. The spectral profile of the eigenmodes, especially the peak frequencies, are sensitive to the choice of model parameters as demonstrated below.

The spatial patterns of the first 5 eigenmodes of $\mathcal{L}(\omega)$, evaluated at the alpha peak of 10 Hz, are shown in Figure 4.1F. Eigenmodes \mathbf{u}_{1-4} produce posterior and temporal spatial patterns, including many elements of the **default mode network**; \mathbf{u}_4 resembles the **sensorimotor network**; and \mathbf{u}_5 the **structural core** of the human connectome. However, these patterns are not exclusive and greatly depend on the frequency at which they are evaluated, as well as the model parameters. Higher eigenmodes are especially sensitive to axonal velocity and frequency (not shown here).

Since the spectral graph model (SGM) relies on connectome topology, we demonstrate in Figure 4.2 that different connectivity matrices produce different frequency responses: A) the individual's structural connectivity matrix, B) HCP average template connectivity matrix, C) uniform connectivity matrix of ones, D) a randomly generated matrix, E) and F) are randomly generated matrices with 75% and 95% sparsity respectively. For Figure 4.2A, optimized parameters for the individual subject's connectome were used. For Figures 4.2B-F, parameters optimized for the HCP template were used. We can observe the spectral profile of the eigenmodes, especially the peak frequencies, are sensitive to the choice of the connectome and the model parameters. All modeled power spectra show a

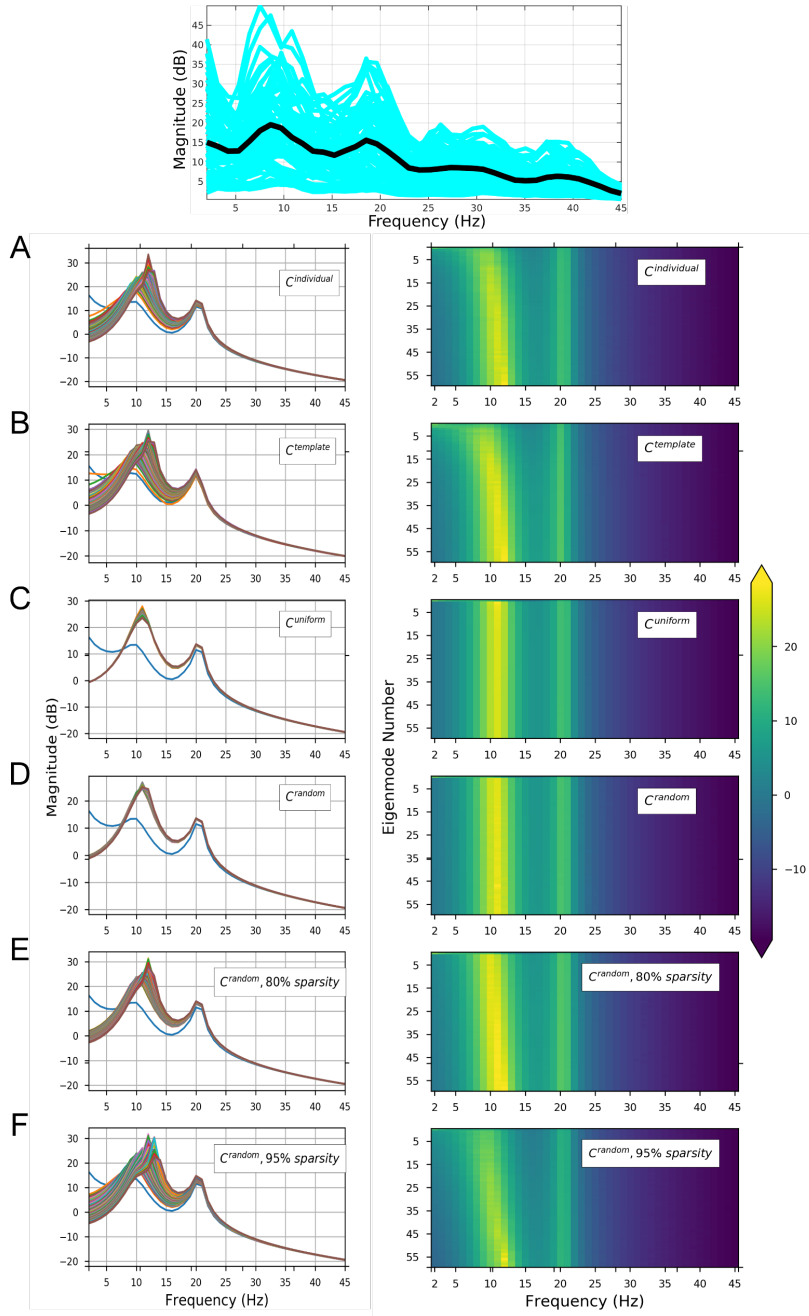


Figure 4.2: Spectral graph model spectra for one subject. Top-Source localized MEG power spectrum for 68 parcellated brain regions. Estimated spectra for each brain region are shown in blue, and average spectrum across all regions is shown in black. The subsequent rows show each eigenmode's spectral magnitude response with model parameters optimized to match the MEG spectrum ($\tau_e = 0.0073$, $\tau_i = 0.0085$, $\tau_G = 0.0061$, $g_{ei} = 2.9469$, $g_{ii} = 4.4865$, $v = 18.3071$, and $\alpha = 0.4639$). Left column shows each eigenmode's frequency responses, while the right column shows the same information as heatmaps. (a) Model using subject's individual structural connectome. (b) Model using average template connectome obtained from 80 HCP subjects. (c) Model using uniform connectivity matrix of ones. (d) Model using randomized connectivity matrix with 75% sparsity. (f) Model using randomized connectivity matrix with 95% sparsity.

broad alpha peak at around 10 Hz and a narrower beta peak at around 20 Hz. This is expected, since these general spectral properties are governed by the local linearized rate model. It is important to note that different eigenmodes accommodate a diversity of frequency responses; for instance, the lowest eigenmodes show a low-frequency response with no alpha peak whatsoever. In all cases the connectome modulates the spectral response in delta-theta range, leaving the higher gamma frequencies unchanged. Particularly, the low eigenmodes ($\mathbf{u}_1 \dots \mathbf{u}_{20}$) appear to modulate the lower frequency range, up to beta, and may be considered responsible for the diversity of spectra observed in the model. In the frequency responses from biologically realistic individual and HCP template connectomes, there is a diversity of spectral responses amongst eigenmodes that is lacking in the response produced by the unrealistic uniform and randomized connectivity matrices. As we will see below, graph topology is critical to the power spectrum it induces, hence we explored whether and how sparsity of random graphs mediates spectral power (Figure 4.2D-F). At incrementally increasing sparsity levels, the diversity of spectral responses of different eigenmodes increases and approaches that of realistic connectomes. Therefore, graph eigenmodes induce unique and diverse frequency responses that depend on the topology of the graph.

4.3.2 Spectral distribution of MEG power depends on model parameters but not connectivity

Network eigenmodes exhibit strong spatial patterning in their frequency responses, even with identical model parameters (Figure 4.3). We evaluated the

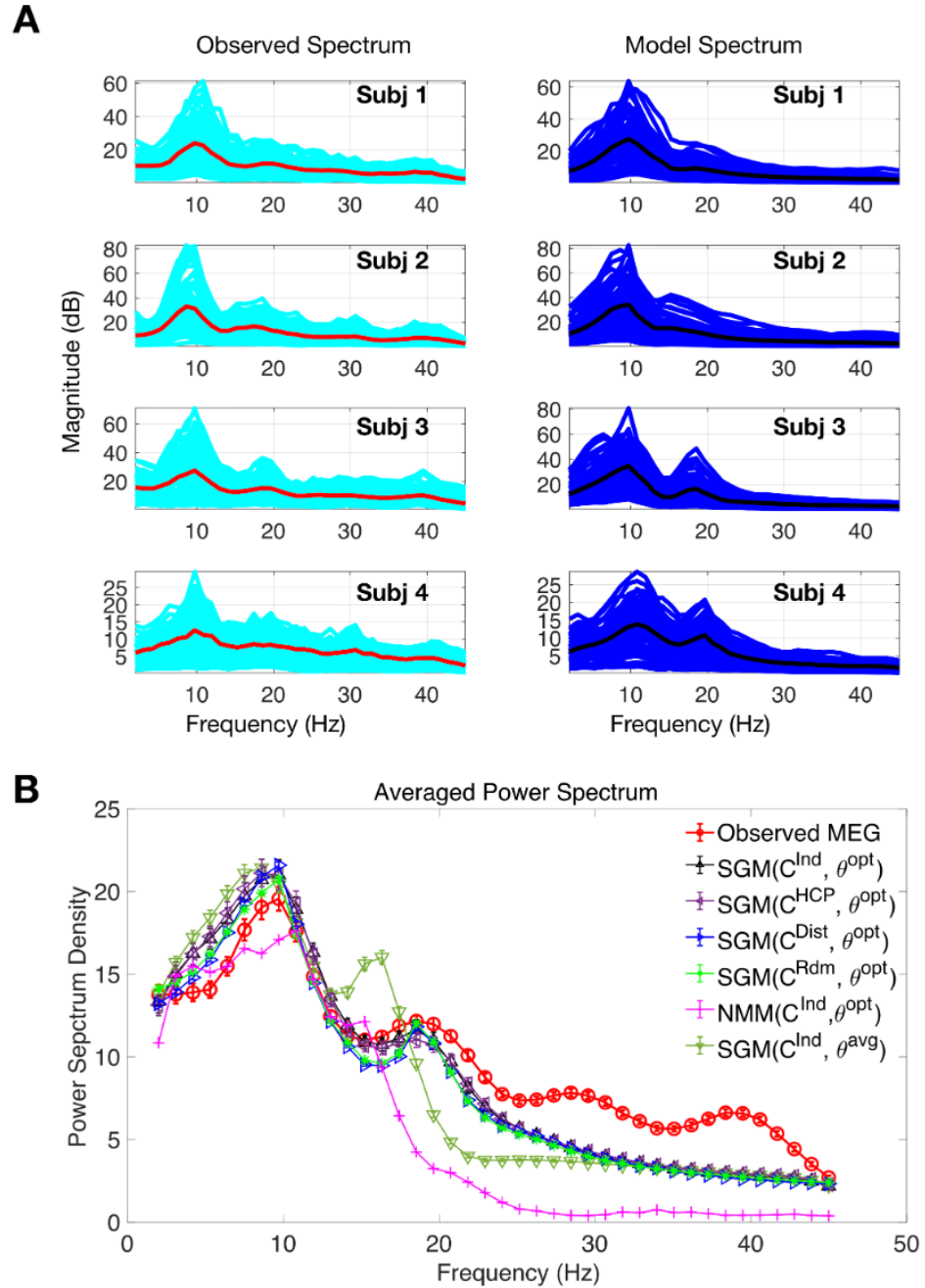


Figure 4.3: Spectral graph model depicts MEG spectra. (a) The observed spectra and SGM's simulated spectra for four representative subjects. Red and cyan curves illustrate source localized empirical average spectra and region-wise spectra respectively. Black and blue curves illustrate simulated average spectra and region-wise spectra respectively. (b) Average observed spectrum across subjects is shown in red. Subsequently, we show average simulated spectra with optimized parameters for individual subject connectomes (black), HCP template connectome (purple), 80% sparse distance connectome (blue), 80% sparse random connectome (green). As a comparison, we also show simulated spectrum with a network neural mass model (pink) and average parameter values and individual connectome (green).

model spectral response using the subject-specific C^{ind} matrices of 4 representative subjects (Figure 4.3A). The model power spectra strikingly resemble empirical MEG spectra, displaying both the alpha and beta peaks on average, and similar regional variability as in real data.

Regional averages of empirical and modeled power spectra of the entire group after full parameter optimization over individual subjects are shown in Figure 4.3B. The model closely replicates the observed power spectrum (red circles) equally well with both C^{ind} (black triangles) and C^{HCP} (purple triangles). Thus, in most cases we can safely replace the subject-specific connectome with the template connectome. In contrast, when non-optimized average parameters were used (golden green triangles), it resulted in a worse fit, especially at high frequencies, suggesting that individualized parameter optimization is essential to produce realistic spectra. We also examined the model behavior for a random connectomes with 80% sparsity (bright green triangles), or a distance-based connectome (blue triangles) was chosen with identical sparsity (80%) to the actual connectome, and found that even with optimized parameters the average spectra could be accounted for by these connectomes.

As another benchmark for comparison, a non-linear network neural mass model [24, 23] (add criticism paper) using our in-house MATLAB implementation, was generally able to produce characteristic alpha and beta frequency peaks, but this model does not resemble empirical wideband spectra. Note that no regionally-varying NMM parameters were used in order to achieve a proper comparison with our model, but both models were optimized with the same algorithm.

Figure 4.4A shows violin plots of the optimized values, indicating that there is

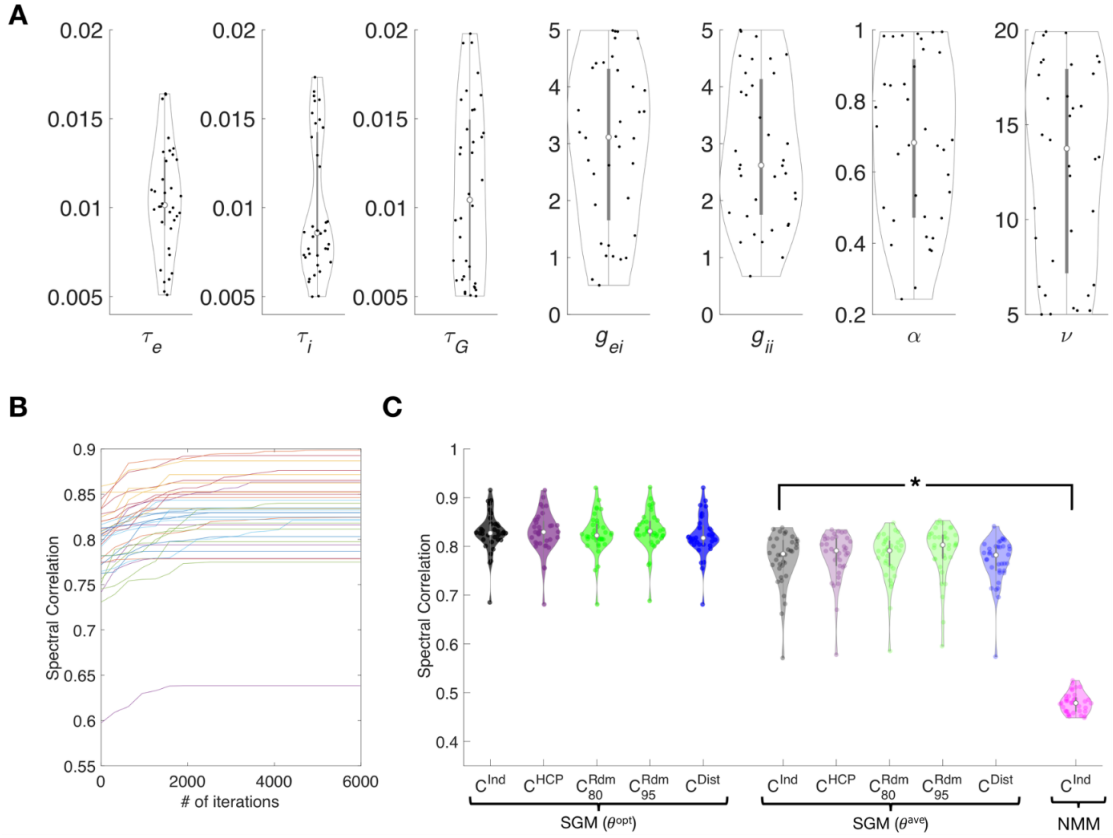


Figure 4.4: Spectral graph model parameter optimization. (a) Distribution of optimized model parameter values across all 36 subjects for parameters $\{\tau_e, \tau_i, \tau_c, g_{ei}, g_{ii}, \alpha, \nu\}$ are shown in violin plots. (b) Performance of optimization algorithm. Spectral Pearson's correlation between simulated and MEG spectra at each iteration. Each curve shows the spectral correlation achieved by the model optimized for a single subject. (c) Distribution of spectral correlation between optimized model and observed spectra across subjects. Correlations with optimized parameters and 5 various connectomes are shown in the left-most columns. Correlations with average parameter values and the same connectomes are shown in the middle section. SGM model outperforms an optimized network NMM regardless of connectome type as denoted by asterisk ($p < 0.001$).

a large range of individually optimal model parameters across subjects. The time constants τ_e, τ_i showed tight clustering but the rest of the parameters showed high variability across subjects. The optimal parameters are in a biologically plausible range, similar to values reported in numerous neural mass models. The optimization algorithm aimed to maximize a cost function proportional to the posterior likelihood of the model, and was quantified by the Pearson's correlation between MEG and modeled spectra ("Spectral correlation"). The

convergence plots shown in Figure 4.4B, one curve for each subject, indicates substantial improvement in cost function from default choice as optimization proceeds. The distribution of optimized spectral correlations is shown in Figure 4.4C. Other model choices were evaluated for comparison: SGM on random connectomes with 80 and 95% sparsity, with and without a distance effect described in Methods, and SGM applied with average optimal model parameters instead of individually optimized ones. In order to test for significance, Fisher's R to z transform was applied, followed by a paired t-test across all subjects between the optimal SGM and other models. The spectral fits for an SGM model with individual connectomes were significantly better than SGM models with average parameters, no matter what connectomes were chosen ($p < 0.001$). Interestingly, spectral fits for SGM model were comparable across all connectomes ($p > .05$). Furthermore, spectral fits for the SGM model were significantly better than that for NMM models with optimized parameters and individual connectome ($p < 1e^{-20}$). Therefore, we conclude that with the graph spectral model, the overall regional spectra appear to be dependent on global model parameters rather than on the actual structural connectome.

4.3.3 Spectral graph model recapitulates the spatial distribution of MEG power

Next, we establish that the model is able to reproduce region-specific spectra, even though it uses identical local oscillations. We integrated the spectral area in the range 8-12 Hz for alpha and 13-25 Hz for beta, of each brain region separately. We define "*spatial correlation*" (as compared to spectral correlation

above) as Pearson's R between the *regional distribution* of empirical MEG and model-predicted power within a given frequency band.

Small number of eigenmodes capture spatial distributions of alpha and beta band activity

We noticed during our experimentation that only a few eigenmodes appear to contribute substantially to observed MEG alpha and beta patterns. Hence we hypothesized that spatial correlations could be improved by selecting a small subset of eigenmodes. Therefore, we developed a sorting strategy whereby we first rank the eigenmodes in descending order of spatial correlation for a given subject and given frequency band. Then we perform summation over only these eigenmodes according to Eq 4.14, each time incrementally adding a new eigenmode to the sum. The spatial correlation of these "sorted-summed" eigenmodes against empirical alpha power are plotted in Figure 4.5C as a function of increasing number of eigenmodes; one curve for each subject. The thick black curve represents the average over all subjects. The spatial correlation initially increases as we add more well-fitting eigenmodes, but peaks around, and begins declining thereafter. Addition of the remaining eigenmodes only serves to reduce the spatial correlation. This behavior is observed in almost all subjects we studied.

Examples of predicted alpha patterns: Figure 4.5 shows brain surface renderings of the spatially distributed patterns of alpha band power for two representative subjects. Regions are color coded as a heatmap of regional power scaled by mean power over all regions. The observed MEG spatial distribution

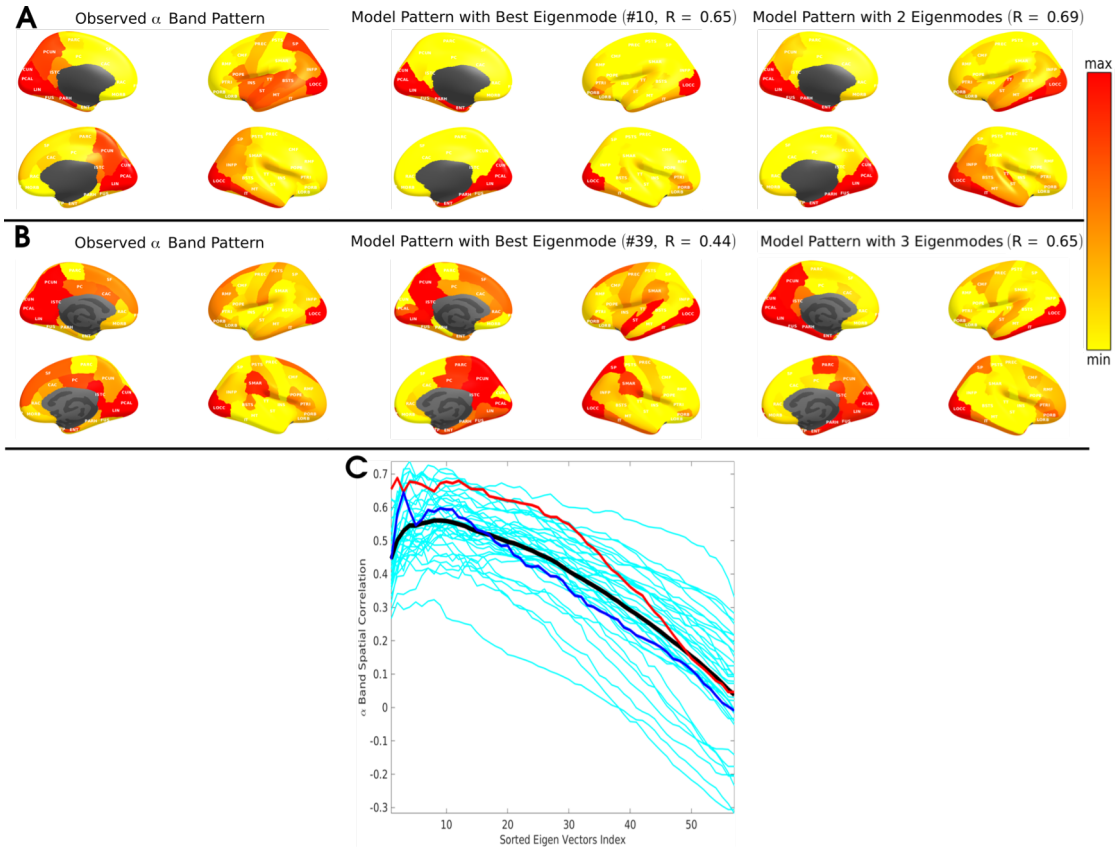


Figure 4.5: Alpha power spatial distribution depicted by specific spectral graph model eigenmodes. (a,b) The spatially distributed patterns of alpha band power for two representative subjects are displayed in brain surface renderings. For each three brain panels shown, the medial surface rendering is shown on the left column while the lateral surface is rendered on the right, the left hemisphere is shown on top and the right hemisphere is shown in the bottom row. Left column: The observed MEG alpha band spatial distribution showing higher power in posterior regions of the brain. Middle column: Spatial distribution of the best matching eigenmode from the SGM. Right column: Spatial distribution of the best cumulative combination of eigenmodes from the SGM. (c) Alpha band spatial correlation for all subjects from SGM simulations with increasing number of cumulative eigenmodes. Individual subject alpha band spatial correlations are shown in cyan ($n = 36$). Panels A and B correspond to the subjects indicated by red and blue curves respectively. Black curve is the average performance across all subjects.

pattern of alpha band shows higher power in posterior regions of the brain, as expected, with strong effect size in temporal, occipital and medial posterior areas. This pattern is matched by one of the eigenmodes (#10, shown in middle panel, giving $R = 0.65$), and slightly better by a weighted combination of 2 eigenmodes ($R = 0.69$). However, the model did not reproduce parietal and parieto-occipital components seen in real data. The other subject produced similar results, but with 6 eigenmodes. In this instance, the parietal component seen in real data were reasonably reproduced by the model.

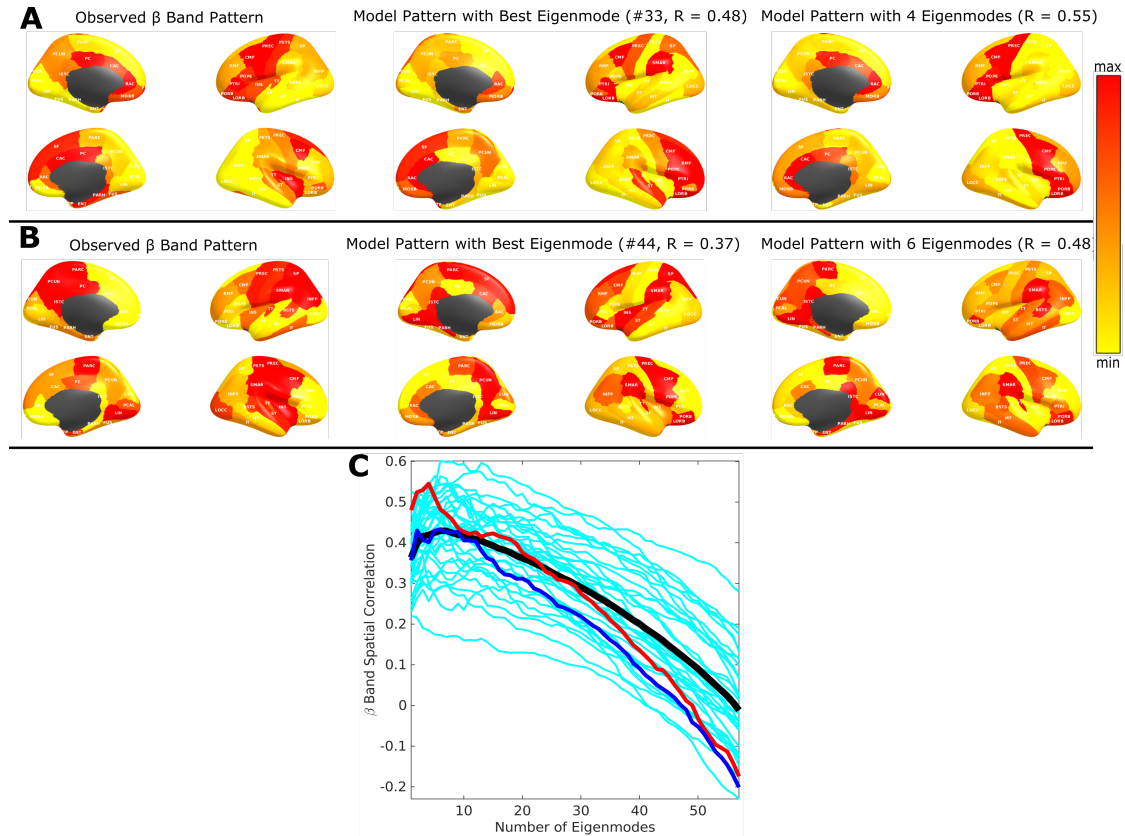


Figure 4.6: Beta power spatial distribution depicted by specific spectral graph model eigenmodes. Legends and layout is identical to Figure 4.5 but shown for beta band spatial distributions.

Examples of predicted beta patterns. Empirical beta power (Figure 4.6, left) is spread throughout the cortex, especially frontal and sensorimotor cortex. A combination of 4 and 6 best matching eigenmodes produced the best model

match to the source localized pattern of two representative subjects, respectively, with $R = 0.55$ and $R = 0.48$. Figure 4.6C shows how the spatial correlation changes as more eigenmodes are used in the "sorted summed" computations, analogous to that of alpha pattern. Here too a peak is achieved for a small number of eigenmodes, typically under 10.

Spatial correlation achieved by the spectral graph model is significantly higher than alternative models

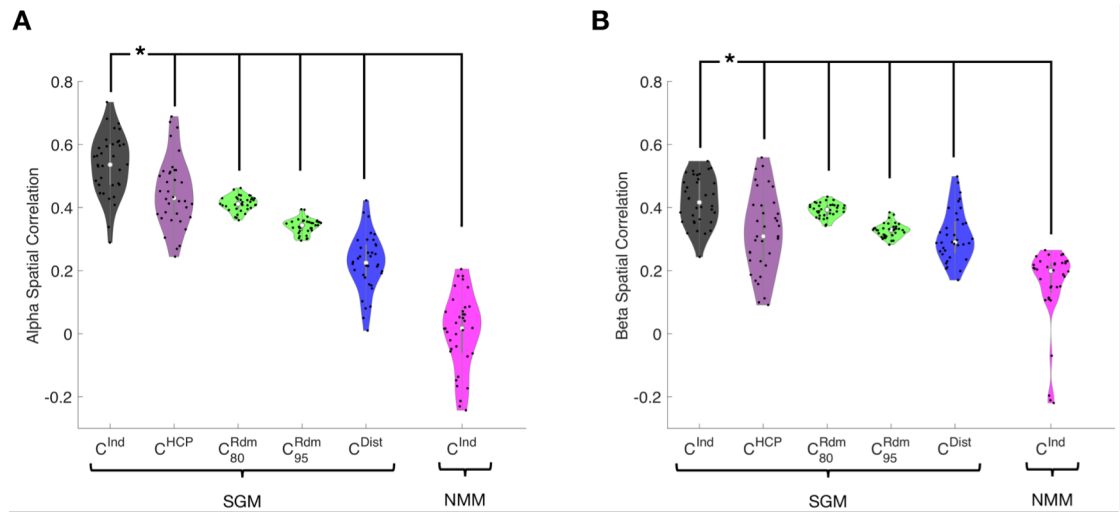


Figure 4.7: Spatial correlation performance of the SGM. Distribution of the SGM for all subjects with the best performing eigenmode. (a) Alpha band spatial correlations. (b) Beta band spatial correlations. For both panels, spatial correlations are shown for SGM with subject individual connectomes (C^{ind} , black), random connectomes with 80% and 95% sparsity (green), geodesic distance based connectome (C^{dist} , blue), and finally for a NMM with specific individual connectome (pink). For each scenario, a selection of the best eigenmodes were obtained for spatial correlation calculations separately. Paired t-tests between $SGM(C^{ind})$ and all other model simulations show that the SGM with individual connectomes significantly outperform all other models; $p < 0.001$ for all alpha spatial correlations and $p < 0.012$ for all beta spatial correlations.

The distribution of peak spatial correlations in the alpha band, using optimized parameters and individual connectomes of all subjects, is plotted in Figure 4.7A. For comparison we show results for four model types: a) SGM

on subject specific individual connectomes (C^{Ind} , black); b) SGM with the HCP template connectome (C^{HCP} , purple); c) SGM on random connectomes with 80% sparsity comparable to individual connectomes or with 95% sparsity where the model shows spectral diversity (C^{Rdm} , green); d) SGM on geodesic distance based connectomes (C^{Dist} , blue); and e) a Wilson-Cowan NMM with subject specific individual connectome (C^{Ind} , pink). Analogous results for beta band spatial correlations are contained in Figure 4.7B. For each connectome model, a selection of the cumulative best set of eigenvectors were separately obtained for spatial correlation calculations. Across all subjects the proposed model, SGM on C^{Ind} , gives excellent spatial correlations in alpha band (R distribution centered at 0.6) as well as in the beta band (R distribution centered at 0.5).

Alternate non-linear model

The Wilson-Cowan neural mass model also did not succeed in predicting the spatial patterns of alpha or beta power, with poor correlations (r centered at 0). This could be because in our implementation we enforced uniform local parameters with no regional variability. However, this is the appropriate comparison, since our proposed model also does not require regionally-varying parameters. Interestingly, the random connectomes and geodesic distance based connectome also appear to have some ability to capture these spatial patterns (R centered at 0.4 and 0.2 respectively), perhaps due to the implicit search for best performing eigenmodes, which on average will give at least a few eigenmodes that look like MEG power purely by chance.

Collectively, we conclude that the graph model is able to fit both the spectral and spatial features of empirical source localized MEG data, and that the optimal

fits performed on individual subjects occurs at widely varying subject-specific parameter choices.

4.4 Discussion

The proposed hierarchical graph spectral model of neural oscillatory activity is a step towards understanding the fundamental relationship between network topology and the macroscopic whole-brain dynamics. The objective is not just to model brain activity phenomenologically, but to analytically derive the mesoscopic laws that drive macroscopic dynamics. This model of the structure-function relationship has the following key distinguishing features: *(a) Hierarchical*: the model’s complexity depends on the level of hierarchy being modeled: complex, non-linear and chaotic dynamics can be accommodated at the local level, but linear graph model is sufficient at the macro-scale. *(b) Graph-based*: Macroscopic dynamics is mainly governed by the connectome, hence linear approximations allow the steady-state frequency response to be specified by the graph Laplacian eigen-decomposition, borrowing heavily from **spectral graph theory** [73, 72, 71, 74]. *(c) Analytic*: The model is available in closed form, without the need for numerical simulations. *(d) Low-dimensional and parsimonious*: Simple, global and universal rules specified with a few parameters, all global and apply at every node, are able to achieve sufficiently complex dynamics. The model is incredibly easy to evaluate, taking no more than a few seconds per brain and to infer model parameters directly from a subject’s MEG data. The optimized model matches observed spectral and spatial patterns in MEG data quite well. No time-consuming simulations of coupled neural masses or chaotic oscillators were needed; indeed, the latter greatly underperformed our model. We report

several novel findings with potentially important implications, discussed below.

4.4.1 Recapitulating regional power spectra at all frequencies

Our main result is the robust demonstration of the model on 36 subjects' MEG data. The representative examples shown in Figures 4.3-4.6 indicate that the graph model recapitulates the observed source localized MEG power spectra for the 68 parcellated brain regions, reproducing the prominent alpha and beta peaks. For each region, the model is also able to predict some characteristics of the full bandwidth power spectra, including what appears to be an inverse power law fall-off over the entire frequency range of interest. However, this aspect will be quantitatively characterized in future work.

We designed a comprehensive parameter optimization algorithm on individual subjects' MEG data of a suitably defined cost function based on Pearson R statistic as a way to capture all relevant spectral features. Using this fitting procedure, we were able to obtain the range of optimally-fitted parameters across the entire study cohort. As shown in Figure 4.4A, the range is broad in most cases, implying that there is significant inter-subject variability of model parameters, even if a template connectome is used for all. We tested the possibility that a group-averaged parameter set might also succeed in matching real spectral data on individuals. But as shown in Figures 4.3B and 4.4C, this was found to be a poor choice, supporting the key role of individual variability of model parameters (but not variability in the connectome). However, no model is capable of reproducing higher frequencies in the higher beta and gamma range seen in MEG, since by design and by biophysical intuition these frequencies arise from

local neural assemblies rather than from modulation by macroscopic networks.

4.4.2 Revealing sources of heterogeneity in spatial patterns of brain activity

The spatial match between model and data is strongest when the model uses empirical macroscopic connectomes obtained from healthy subjects' diffusion weighted MRI scans, followed by tractography. The use of "null" connectomes - randomized connectivity matrices of varying levels of sparsity and distance-based connectivity matrices, respectively, did far worse than actual human connectomes (Figure 4.7), supporting the fact that the latter is the key mediator of spatial patterns of real brain activity. The match was also significantly different when using a template HCP connectome versus the individual subject's own connectomes, and when compared to spatial patterns predicted by an NMM. In conclusion, for the purpose of predicting the spatial topography of brain activity, it is important to use individual connectomes and optimized model parameters.

4.4.3 Macroscopic brain rhythms are governed by the connectome

A predominant view assumes that different brain rhythms are produced by groups of neurons with similar characteristic frequencies, which might synchronize and act as "pacemakers". How could this view explain why alpha and beta power are spatially stereotyped across subjects, and why the alpha signal is espe-

cially prominent in posterior areas? Although practically any computer model of cortical activity can be tuned, with suitable parameter choice, to oscillate at alpha frequency, e.g. [44, 55, 58, 60, 70, 91, 92], none of them are able to parsimoniously recapitulate the posterior origin of alpha. Thus the prominence of posterior alpha might be explained by the hypothesized existence of alpha generators in posterior areas. Indeed, most oscillator models of local dynamics are capable of producing these rhythms at any desired frequency [44, 70, 93, 94, 30], and therefore it is common to tweak their parameters to reproduce alpha rhythm. Local networks of simulated multicompartmental neurons can produce oscillations in the range 8–20 Hz [44], and, in a non-linear continuum theory, peaks at various frequencies in the range 2–16Hz were obtained depending on the parameters [94]. Specifically, the role of thalamus as pacemaker has motivated thalamocortical models [50, 55] that are capable of resonances in various ranges. Neural field models of the thalamocortical loop [55] can also predict slow-wave and spindle oscillations in sleep, and alpha, beta, and higher-frequency oscillations in the waking state. In these thalamocortical models, the posterior alpha can arise by postulating a differential effect in weights of the posterior versus anterior thalamic projections, e.g. [92]. Ultimately, hypotheses requiring local rhythm generators suffer from lack of parsimony and specificity: a separate pacemaker must be postulated for each spectral peak at just the right location [95].

An alternative view emerges from our results that macroscopic brain rhythms are governed by the structural connectome. Even with global model parameters, using the exact same local cortical dynamics captured by the local transfer function $H_{local}(\omega)$, driven by identically distributed random noise $\mathbf{P}(\omega)$, our model is capable of predicting prominent spectral (Figures 4.2, 4.3) and spatial (Figures 4.5, 4.6) patterning that is quite realistic. This is especially true in the lower fre-

quency range: indeed, the model is able to predict not just the frequency spectra in alpha and beta ranges, but also their spatial patterns – i.e. posterior alpha and distributed but roughly frontal beta. Although this is not definitive proof, it raises the intriguing possibility that the macroscopic spatial distribution of the spectra of brain signals *does not require spatial heterogeneity of local signal sources, nor regionally variable parameters*. Rather, it implies that the most prominent *patterning of brain activity (especially alpha) may be governed by the topology of the macroscopic network* rather than by local, regionally-varying drivers. Nevertheless, a deeper exploration is required of the topography of the dominant eigenmodes of our linear model, in order to understand the spatial gradients postulated previously [55, 92].

4.4.4 Emergence of linearity from chaotic brain dynamics

The non-linear and chaotic dynamics of brain signals may at first appear to preclude deterministic or analytic modeling of any kind. Yet, vast swathes of neuroscientific terrain are surprisingly deterministic, reproducible and conserved across individuals and even species. Brain rhythms generally fall within identical frequency bands and spatial maps [43, 55, 68]. Based on the hypothesis that the emergent behavior of long-range interactions can be independent of detailed local dynamics of individual neurons [52, 53, 54, 56, 31], and may be largely governed by long-range connectivity [57, 58, 59, 60], we have reported here a minimal linear model of how the brain connectome serves as a spatial-spectral filter that modulates the underlying non-linear signals emanating from local circuits. Nevertheless, we recognize the limitations of a linear model and its inability to capture inherent non-linearities across all levels in the system.

4.4.5 Relationship to other work

One can view the proposed generative model as a biophysical realization of a dynamic causal model (DCM) [96, 97, 98, 99, 100] for whole brain electrophysiological activity but with very different goals, model dimensionality and inference procedures.

First, the goal of many prior efforts using DCMs is to examine effective connectivity in EEG, LFP and fMRI functional connectivity data, typically for smaller networks[100, 101], or dynamic effective connectivity[102, 103, 104]. Hence, they address the second order covariance structures of brain activity. In particular, recent spectral DCM and regression DCM models [105, 106, 107] with local neural masses are formulated in the steady-state frequency-domain, and the resulting whole-brain cross-spectra are evaluated. The goals of these models are to derive model cross-spectra that define the effective connectivity in the frequency domain and are compared with empirical cross-spectra. Based on second-order sufficient statistics, these models attempt to derive effective connectivity from functional connectivity data. These DCMs have so far only been applied to small networks or to BOLD fMRI regime. In contrast, our goal is to examine the role of the eigenmodes of the structural connectome and their influence on power spectral distributions in the full MEG frequency range, and over the entire whole brain. In subsequent work, we intend to extend our efforts to examining effective connectivity but such an effort currently remains outside the scope of the work in this paper. Here, we focus on models that directly estimate the first order effects of observed power spectra and its spatial distributions and compare them with empirical MEG source reconstructions. Our primary motivation is to examine whether spatial distribution of observed power

spectra can arise from graph structure of the connectome, hence our focus on the effects of model behavior as a function of the underlying structural connectome – whether it is individualized, template-based, uniform, random or distance based. DCM methods have not reported first order regional power spectra as we do here, nor have they explored how the structural connectome influences model spectral distributions.

Second, our model is more parsimonious compared to most of these above-mentioned models which have many more degrees of freedom because they often allow for regions and their interactions to have different parameters. Our model parameterization, with only a few global parameters, lends itself to efficient computations over fine-scale whole-brain parcellations, whereas most DCMs (with the exception of recent spectral and regression DCMS[105, 106, 107]) are suited for examining smaller networks but involve large effective connectivity matrices and region-specific parameters. Furthermore, parameters of our model remain grounded and interpretable in terms of the underlying biophysics, i.e. time constants and conductivities. In contrast, spectral and regression DCM models of cross-spectra have parameters that are abstract and do not have immediate biophysical interpretation.

The third major difference is in the emphasis placed on Variational Bayesian inference in DCM. Since our focus was on exploring model behavior over a small number of global parameters and a set of structural connectomes (whether anatomic or random) of identical sparsity and complexity, it was sufficient to use a *maximum a posteriori* (MAP) estimation procedure for Bayesian inference of our global model parameters with flat non-informative priors with pre-determined ranges based on biophysics. Like most DCM efforts our model can be easily be

extended to Variational Empirical Bayesian inference for parameter estimation, for instance to compute a full posterior of the structural connectivity matrix. In such a formulation, we can assume that the observed structural connectome will serve as the prior mean of the connectivity matrix. We reserve such extensions to our future work with this spectral graph model.

4.4.6 Other limitations and extensions

The model currently examines resting-state activity, but future extensions will include prediction of functional connectivity, task-induced modulations of neural oscillations and causal modeling of external stimuli, e.g. transcranial magnetic and direct current stimulation. The current implementation does not incorporate complex local dynamics, but future work will explore using non-white internal noise and chaotic dynamics for local assemblies. This may allow us to examine higher gamma frequencies. Although our model incorporates latency information derived from path distances, we plan to explore path-specific propagation velocities derived from white matter microstructural metrics such as axon diameter distributions and myelin thickness. Future work will also examine the specific topographic features of the structural connectome that may best describe canonical neural activity spectra. Finally, we plan to examine the ability of the model to predict time-varying structure-function relationships.

4.4.7 Potential applications

Mathematical encapsulation of the structure-function relationship can potentiate

novel approaches for mapping and monitoring brain diseases such as autism, schizophrenia, epilepsy and dementia, since early functional changes are more readily and sensitively measured using fMRI and MEG, compared to structural changes. Because of the complementary sensitivity, temporal and spatial resolutions of diffusion MRI, MEG, EEG and fMRI, combining these modalities may be able to reveal fine spatiotemporal structures of neuronal activity that would otherwise remain undetected if using only one modality. Current efforts at fusing multimodalities are interpretive, phenomenological or statistical, with limited cognizance of underlying neuronal processes. Thus, the ability of the presented model to quantitatively and parsimoniously capture the structure-function relationship may be key to achieving true multi-modality integration.

CHAPTER 5

CHAPTER 3

CHAPTER 6

CHAPTER 4

APPENDIX A

CHAPTER 1 OF APPENDIX

Appendix chapter 1 text goes here

BIBLIOGRAPHY

- [1] David J. Sharp, Christian F. Beckmann, Richard Greenwood, Kirsi M. Kin-nunen, Valerie Bonnelle, Xavier De Boissezon, Jane H. Powell, Serena J. Counsell, Maneesh C. Patel, and Robert Leech. Default mode network functional and structural connectivity after traumatic brain injury. *Brain: A Journal of Neurology*, 134(Pt 8):2233–2247, August 2011.
- [2] Xilin Shen, Emily S. Finn, Dustin Scheinost, Monica D. Rosenberg, Marvin M. Chun, Xenophon Papademetris, and R. Todd Constable. Using connectome-based predictive modeling to predict individual behavior from brain connectivity. *Nature Protocols*, 12(3):506–518, March 2017.
- [3] Quentin J. M. Huys, Tiago V. Maia, and Michael J. Frank. Computational psychiatry as a bridge from neuroscience to clinical applications. *Nature Neuroscience*, 19(3):404–413, March 2016.
- [4] Eleftherios Garyfallidis, Matthew Brett, Bagrat Amirbekian, Ariel Rokem, Stefan Van Der Walt, Maxime Descoteaux, and Ian Nimmo-Smith. Dipy, a library for the analysis of diffusion mri data. *Frontiers in Neuroinformatics*, 8:8, 2014.
- [5] Jeffrey I. Berman, SungWon Chung, Pratik Mukherjee, Christopher P. Hess, Eric T. Han, and Roland G. Henry. Probabilistic streamline q-ball tractog-raphy using the residual bootstrap. *NeuroImage*, 39(1):215–222, January 2008.
- [6] Ariel Rokem, Jason D. Yeatman, Franco Pestilli, Kendrick N. Kay, Aviv Mezer, Stefan van der Walt, and Brian A. Wandell. Evaluating the accuracy of diffusion mri models in white matter. *PLOS ONE*, 10(4):e0123272, April 2015.
- [7] Eleftherios Garyfallidis, Nahla E, and Yu-Chien Wu. Superresolved HYDI dataset. 11 2019.
- [8] Nahla M H Elsaïd, Pierrick Coupé, and Yu-Chien Wu. Super-resolution hy-brid diffusion imaging (sr-hydi). *International Society for Magnetic Resonance in Medicine (ISMRM)*, 2019.
- [9] A. L. Hodgkin and A. F. Huxley. A quantitative description of membrane current and its application to conduction and excitation in nerve. *The Journal of Physiology*, 117:500–544, 1952.

- [10] Ed Bullmore and Olaf Sporns. Complex brain networks: graph theoretical analysis of structural and functional systems. *Nature Reviews Neuroscience*, 10(3):186–198, March 2009.
- [11] Rahul S. Desikan, Florent Segonne, Bruce Fischl, Brian T. Quinn, Bradford C. Dickerson, Deborah Blacker, Randy L. Buckner, Anders M. Dale, R. Paul Maguire, Bradley T. Hyman, Marilyn S. Albert, and Ronald J. Killiany. An automated labeling system for subdividing the human cerebral cortex on mri scans into gyral based regions of interest. *NeuroImage*, 31:968–980, 2006.
- [12] R. Cameron Craddock, G. Andrew James, Paul E. Holtzheimer, Xiaoping P. Hu, and Helen S. Mayberg. A whole brain fMRI atlas generated via spatially constrained spectral clustering. *Human brain mapping*, 33, 2012.
- [13] Danielle S. Bassett and Edward T. Bullmore. Human brain networks in health and disease. *Current Opinion in Neurology*, 22:340–347, August 2009.
- [14] Miao Cao, Jin-Hui Wang, Zheng-Jia Dai, Xiao-Yan Cao, Li-Li Jiang, Feng-Mei Fan, Xiao-Wei Song, Ming-Rui Xia, Ni Shu, Qi Dong, Michael P. Milham, F. Xavier Castellanos, Xi-Nian Zuo, and Yong He. Topological organization of the human brain functional connectome across the lifespan. *Developmental Cognitive Neuroscience*, 7, 2014.
- [15] Nivedita Chatterjee and Sitabhra Sinha. Understanding the mind of a worm: hierarchical network structure underlying nervous system function in *c. elegans*. *Progress in Brain Research*, 168:145–153, 2008.
- [16] Danielle Smith Bassett and Ed Bullmore. Small-world brain networks. *The Neuroscientist*, pages 512–523, 2006.
- [17] Y. He, Z. Chen, and A. Evans. Structural insights into aberrant topological patterns of large-scale cortical networks in alzheimer’s disease. *Journal of Neuroscience*, 28:4756–4766, 2008.
- [18] R. L. Buckner. Molecular, structural, and functional characterization of alzheimer’s disease: Evidence for a relationship between default activity, amyloid, and memory. *Journal of Neuroscience*, 25:7709–7717, 2005.
- [19] N Brunel and N Brunel. Dynamics of sparsely connected networks of excitatory and inhibitory neurons. *Computational Neuroscience*, 8:183–208, 2000.

- [20] Nicolas Brunel and Xiao Jing Wang. Effects of neuromodulation in a cortical network model of object working memory dominated by recurrent inhibition. *Journal of Computational Neuroscience*, 11:63–85, 2001.
- [21] Laura E. Suárez, Ross D. Markello, Richard F. Betzel, and Bratislav Misic. Linking structure and function in macroscale brain networks. *Trends in Cognitive Sciences*, 24:302–315, 2020-04-01.
- [22] Shi Gu, Fabio Pasqualetti, Matthew Cieslak, Qawi K. Telesford, Alfred B. Yu, Ari E. Kahn, John D. Medaglia, Jean M. Vettel, Michael B. Miller, Scott T. Grafton, and Danielle S. Bassett. Controllability of structural brain networks. *Nature Communications*, 6:8414, 2015.
- [23] Sarah Feldt Muldoon, Fabio Pasqualetti, Shi Gu, Matthew Cieslak, Scott T. Grafton, Jean M. Vettel, and Danielle S. Bassett. Stimulation-based control of dynamic brain networks. *PLOS Computational Biology*, 12(9):1–23, 2016.
- [24] H R Wilson and J D Cowan. Excitatory and inhibitory interactions in localized populations of model neurons. *Biophysical journal*, 12(1):1–24, 1972.
- [25] Sami El Boustani and Alain Destexhe. A master equation formalism for macroscopic modeling of asynchronous irregular activity states. *Neural computation*, 21(1):46–100, 2009.
- [26] Paul L. Nunez. The brain wave equation: a model for the EEG. *Mathematical Biosciences*, 21(3):279–297, 1974.
- [27] V. K. Jirsa and H. Haken. A derivation of a macroscopic field theory of the brain from the quasi-microscopic neural dynamics. *Physica D: Nonlinear Phenomena*, 99(4):503–526, 1997-01-01.
- [28] P. A. Valdes, J. C. Jimenez, J. Riera, R. Biscay, and T. Ozaki. Nonlinear EEG analysis based on a neural mass model. *Biological Cybernetics*, 81(5):415–424, 1999.
- [29] C. J. Honey, O. Sporns, L. Cammoun, X. Gigandet, J. P. Thiran, R. Meuli, and P. Hagmann. Predicting human resting-state functional connectivity from structural connectivity. *Proceedings of the National Academy of Sciences*, 106(6):2035–2040, February 2009.
- [30] A. Spiegler and V. Jirsa. Systematic approximations of neural fields through

- networks of neural masses in the virtual brain. *NeuroImage*, 83(March):704–725, 2013.
- [31] Farras Abduelnour, Henning U. Voss, and Ashish Raj. Network diffusion accurately models the relationship between structural and functional brain connectivity networks. *NeuroImage*, 90:335–347, 2014.
- [32] Selen Atasoy, Isaac Donnelly, and Joel Pearson. Human brain networks function in connectome-specific harmonic waves. *Nature Communications*, 7(1):10340, April 2016.
- [33] Prejaas Tewarie, Romesh Abeysuriya, Aine Byrne, George C. O'Neill, Stamatios N. Sotiropoulos, Matthew J. Brookes, and Stephen Coombes. How do spatially distinct frequency specific MEG networks emerge from one underlying structural connectome? the role of the structural eigenmodes. *NeuroImage*, 186:211–220, 2019.
- [34] Ashish Raj, Chang Cai, Xihe Xie, Eva Palacios, Julia Owen, Pratik Mukherjee, and Srikantan Nagarajan. Spectral graph theory of brain oscillations. *Human Brain Mapping*, 41(11):1–19, 2020.
- [35] Farras Abduelnour, Michael Dayan, Orrin Devinsky, Thomas Thesen, and Ashish Raj. Functional brain connectivity is predictable from anatomic network's laplacian eigen-structure. *NeuroImage*, 172:728–739, 2018.
- [36] Ian Stewart. Holes and hot spots. *Nature*, 401:863–865, 1999.
- [37] P. A. Robinson, X. Zhao, K. M. Aquino, J. D. Griffiths, S. Sarkar, and Grishma Mehta-Pandejee. Eigenmodes of brain activity: Neural field theory predictions and comparison with experiment. *NeuroImage*, 142:79–98, 2016.
- [38] Maria Giulia Preti and Dimitri Van De Ville. Decoupling of brain function from structure reveals regional behavioral specialization in humans. *Nature Communications*, 10, 2019.
- [39] B T Thomas Yeo, Fenna M Krienen, Jorge Sepulcre, Mert R Sabuncu, Danial Lashkari, Marisa Hollinshead, Joshua L Roffman, Jordan W Smoller, Lilla Zöllei, Jonathan R Polimeni, Bruce Fischl, Hesheng Liu, and Randy L Buckner. The organization of the human cerebral cortex estimated by intrinsic functional connectivity. *Journal of neurophysiology*, 106:1125–65, 2011.

- [40] A.P. French. *Vibrations and Waves*. M.I.T. introductory physics series. Taylor & Francis, 1971.
- [41] Patric Hagmann, Leila Cammoun, Xavier Gigandet, Reto Meuli, Christopher J. Honey, Van J. Wedeen, and Olaf Sporns. Mapping the structural core of human cerebral cortex. *PLOS Biology*, 6(7):e159, July 2008.
- [42] Yasser Iturria-Medina. Anatomical brain networks on the prediction of abnormal brain states. *Brain connectivity*, 3(1):1–21, January 2013.
- [43] Walter J. Freeman and Jian Zhai. Simulated power spectral density (psd) of background electrocorticogram (ecog). *Cognitive Neurodynamics*, 3(1):97–103, March 2009.
- [44] D T J Liley, D M Alexander, J J Wright, and M D Aldous. Alpha rhythm emerges from large-scale networks of realistically coupled multicompartmental model cortical neurons. *Network-Computation In Neural Systems*, 10(1):79–92, 1999.
- [45] Per E. Roland, Claus C. Hilgetag, and Gustavo Deco. Tracing evolution of spatio-temporal dynamics of the cerebral cortex: cortico-cortical communication dynamics. *Frontiers in Systems Neuroscience*, 8:76, 2014.
- [46] Valentin Markounikau, Christian Igel, Amiram Grinvald, and Dirk Jancke. A dynamic neural field model of mesoscopic cortical activity captured with voltage-sensitive dye imaging. *PLOS Computational Biology*, 6(9):e1000919, September 2010.
- [47] Evan S. Schaffer, Srdjan Ostoic, and L. F. Abbott. A complex-valued firing-rate model that approximates the dynamics of spiking networks. *PLOS Computational Biology*, 9(10):e1003301, October 2013.
- [48] Henry Markram. The Blue Brain Project. *Nature Reviews Neuroscience*, 7(2):153–160, February 2006.
- [49] Henry Markram, Eilif Muller, Srikanth Ramaswamy, Michael W. Reimann, Marwan Abdellah, Carlos Aguado Sanchez, Anastasia Ailamaki, Lidia Alonso-Nanclares, Nicolas Antille, Selim Arsever, Guy Antoine Atenekeng Kahou, Thomas K. Berger, Ahmet Bilgili, Nenad Buncic, Athanassia Chalimourda, Giuseppe Chindemi, Jean-Denis Courcol, Fabien Delalondre, Vincent Delattre, Shaul Druckmann, Raphael Dumusc, James Dynes, Stefan Eilemann, Eyal Gal, Michael Emiel Gevaert, Jean-Pierre Ghobril, Albert Gidon, Joe W. Graham, Anirudh Gupta, Valentin Haenel, Etay Hay, Thomas

Heinis, Juan B. Hernando, Michael Hines, Lida Kanari, Daniel Keller, John Kenyon, Georges Khazen, Yihwa Kim, James G. King, Zoltan Kisvarday, Pramod Kumbhar, Sébastien Lasserre, Jean-Vincent Le Bé, Bruno R. C. Magalhães, Angel Merchán-Pérez, Julie Meystre, Benjamin Roy Morrice, Jeffrey Muller, Alberto Muñoz-Céspedes, Shruti Muralidhar, Keerthan Muthurasa, Daniel Nachbaur, Taylor H. Newton, Max Nolte, Aleksandr Ovcharenko, Juan Palacios, Luis Pastor, Rodrigo Perin, Rajnish Ranjan, Imad Riachi, José-Rodrigo Rodríguez, Juan Luis Riquelme, Christian Rössert, Konstantinos Sfyrakis, Ying Shi, Julian C. Shillcock, Gilad Silberberg, Ricardo Silva, Farhan Tauheed, Martin Telefont, Maria Toledo-Rodriguez, Thomas Tränkler, Werner Van Geit, Jafet Villafranca Díaz, Richard Walker, Yun Wang, Stefano M. Zaninetta, Javier DeFelipe, Sean L. Hill, Idan Segev, and Felix Schürmann. Reconstruction and simulation of neocortical microcircuitry. *Cell*, 163(2):456–492, October 2015.

- [50] Eugene M. Izhikevich and Gerald M. Edelman. Large-scale model of mammalian thalamocortical systems. *Proceedings of the National Academy of Sciences*, 105(9):3593–3598, March 2008.
- [51] Tobias C. Potjans and Markus Diesmann. The cell-type specific cortical microcircuit: relating structure and activity in a full-scale spiking network model. *Cerebral Cortex (New York, N.Y.: 1991)*, 24(3):785–806, March 2014.
- [52] H. Shimizu and H. Haken. Co-operative dynamics in organelles. *Journal of Theoretical Biology*, 104(2):261–273, September 1983.
- [53] Bratislav Mišić, Olaf Sporns, and Anthony R. McIntosh. Communication efficiency and congestion of signal traffic in large-scale brain networks. *PLoS Computational Biology*, 10(1), 2014.
- [54] Bratislav Mišić, Richard F. Betzel, Azadeh Nematzadeh, Joaquin Goñi, Alessandra Griffa, Patric Hagmann, Alessandro Flammini, Yong Yeol Ahn, and Olaf Sporns. Cooperative and competitive spreading dynamics on the human connectome. *Neuron*, 86(6):1518–1529, 2015.
- [55] P a Robinson, C J Rennie, D L Rowe, S C O'Connor, E Gordon, S C O Connor, and E Gordon. Multiscale brain modelling. *Philosophical transactions of the Royal Society of London. Series B, Biological sciences*, 360(1457):1043–50, 2005.
- [56] Alain Destexhe and Terrence J. Sejnowski. The wilson-cowan model, 36 years later. *Biological Cybernetics*, 101(1):1–2, 2009.

- [57] F Abdelnour, A Raj, M Dayan, O Devinsky, and T Thesen. Estimating function from structure in epileptics using graph diffusion model. In *2015 IEEE 12th International Symposium on Biomedical Imaging (ISBI)*, pages 466–469, April 2015.
- [58] Tristan T Nakagawa, Mark Woolrich, Henry Luckhoo, Morten Joensson, Hamid Mohseni, Morten L Kringelbach, Viktor Jirsa, and Gustavo Deco. How delays matter in an oscillatory whole-brain spiking-neuron network model for MEG alpha-rhythms at rest. *NeuroImage*, 87:383–94, February 2014.
- [59] V.K. Jirsa, K.J. Jantzen, A. Fuchs, and J.A.S. Kelso. Spatiotemporal forward solution of the eeg and meg using network modeling. *IEEE Transactions on Medical Imaging*, 21(5):493–504, May 2002.
- [60] Gustavo Deco, Mario Senden, and Viktor Jirsa. How anatomy shapes dynamics: a semi-analytical study of the brain at rest by a simple spin model. *Frontiers in computational neuroscience*, 6:68, January 2012.
- [61] Sophie Achard, Raymond Salvador, Brandon Whitcher, John Suckling, and Ed Bullmore. A resilient, low-frequency, small-world human brain functional network with highly connected association cortical hubs. *The Journal of neuroscience : the official journal of the Society for Neuroscience*, 26(1):63–72, January 2006.
- [62] Steven H. Strogatz. Exploring complex networks. *Nature*, 410(6825):268–76, March 2001.
- [63] Martijn P. van den Heuvel, René C. W. Mandl, René S. Kahn, and Hilleke E. Hulshoff Pol. Functionally linked resting-state networks reflect the underlying structural connectivity architecture of the human brain. *Human Brain Mapping*, 30(10):3127–3141, October 2009.
- [64] Ann M. Hermundstad, Danielle S. Bassett, Kevin S. Brown, Elissa M. Aminoff, David Clewett, Scott Freeman, Amy Frithsen, Arianne Johnson, Christine M. Tipper, Michael B. Miller, Scott T. Grafton, and Jean M. Carlson. Structural foundations of resting-state and task-based functional connectivity in the human brain. *Proceedings of the National Academy of Sciences of the United States of America*, 110(15):6169–6174, April 2013.
- [65] Mikail Rubinov, Olaf Sporns, Cees van Leeuwen, and Michael Breakspear. Symbiotic relationship between brain structure and dynamics. *BMC Neuroscience*, 10(1):55, June 2009.

- [66] A. Ghosh, Y. Rho, A. R. McIntosh, R. Kötter, and V. K. Jirsa. Cortical network dynamics with time delays reveals functional connectivity in the resting brain. *Cognitive Neurodynamics*, 2(2):115, April 2008.
- [67] Hae-Jeong Park and Karl Friston. Structural and functional brain networks: from connections to cognition. *Science (New York, N.Y.)*, 342(6158):1238411, November 2013.
- [68] Biyu J. He, John M. Zempel, Abraham Z. Snyder, and Marcus E. Raichle. The temporal structures and functional significance of scale-free brain activity. *Neuron*, 66(3):353–369, May 2010.
- [69] H. R. Wilson and J. D. Cowan. A mathematical theory of the functional dynamics of cortical and thalamic nervous tissue. *Kybernetik*, 13(2):55–80, September 1973.
- [70] Olivier David and Karl J. Friston. A neural mass model for meg/eeg: coupling and neuronal dynamics. *NeuroImage*, 20(3):1743–1755, November 2003.
- [71] Rasmus Larsen, Mads Nielsen, Jon Sporring, Fan Zhang, and Edwin Hancock. *Medical Image Computing and Computer-Assisted Intervention – MICCAI 2006*, volume 4191. Springer Berlin Heidelberg, Berlin, Heidelberg, 2006.
- [72] Risi Imre Kondor and John Lafferty. Diffusion kernels on graphs and other discrete structures. In *In Proceedings of the ICML*, pages 315–322, 2002.
- [73] Benjamin Auffarth. Spectral graph clustering. *Universitat de Barcelona, course report for*, pages 1–12, 2007.
- [74] Andrew Y. Ng, Michael I. Jordan, and Yair Weiss. On spectral clustering: Analysis and an algorithm. In *ADVANCES IN NEURAL INFORMATION PROCESSING SYSTEMS*, pages 849–856. MIT Press, 2001.
- [75] Roberto F. Galán. On How Network Architecture Determines the Dominant Patterns of Spontaneous Neural Activity. *PLOS ONE*, 3(5):e2148, May 2008.
- [76] Joaquín Goñi, Martijn P. van den Heuvel, Andrea Avena-Koenigsberger, Nieves Velez de Mendizabal, Richard F. Betzel, Alessandra Griffa, Patric Hagmann, Bernat Corominas-Murtra, Jean-Philippe Thiran, and Olaf

- Sporns. Resting-brain functional connectivity predicted by analytic measures of network communication. *Proceedings of the National Academy of Sciences*, 111(2):833–838, January 2014.
- [77] Maxwell B. Wang, Julia P. Owen, Pratik Mukherjee, and Ashish Raj. Brain network eigenmodes provide a robust and compact representation of the structural connectome in health and disease. *PLOS Computational Biology*, 13(6):e1005550, June 2017.
 - [78] Farras Abdnour, Susanne Mueller, and Ashish Raj. Relating cortical atrophy in temporal lobe epilepsy with graph diffusion-based network models. *PLOS Computational Biology*, 11(10):e1004564, October 2015.
 - [79] Farras Abdnour, Ashish Raj, Orrin Devinsky, and Thomas Thesen. Network analysis on predicting mean diffusivity change at group level in temporal lobe epilepsy. *Brain Connectivity*, 6(8):607–620, October 2016.
 - [80] Ashish Raj, Amy Kuceyeski, and Michael Weiner. A network diffusion model of disease progression in dementia. *Neuron*, 73(6):1204–1215, March 2012.
 - [81] Isabelle Ferezou, Florent Haiss, Luc J. Gentet, Rachel Aronoff, Bruno Weber, and Carl C. H. Petersen. Spatiotemporal Dynamics of Cortical Sensorimotor Integration in Behaving Mice. *Neuron*, 56(5):907–923, December 2007.
 - [82] Pierre-Olivier Polack and Diego Contreras. Long-Range Parallel Processing and Local Recurrent Activity in the Visual Cortex of the Mouse. *The Journal of Neuroscience*, 32(32):11120–11131, August 2012.
 - [83] Bruce Fischl, David H Salat, Evelina Busa, Marilyn Albert, Megan Deterich, Christian Haselgrove, Andre Van Der Kouwe, Ron Killiany, David Kennedy, Shuna Klaveness, Albert Montillo, Nikos Makris, Bruce Rosen, and Anders M Dale. Whole brain segmentation: Automated labeling of neuroanatomical structures in the human brain. *Neuron*, 33:341–355, 2002.
 - [84] Julia P. Owen, Yi-Ou Li, Etay Ziv, Zoe Strominger, Jacquelyn Gold, Polina Bukhpun, Mari Wakahiro, Eric J. Friedman, Elliott H. Sherr, and Pratik Mukherjee. The structural connectome of the human brain in agenesis of the corpus callosum. *NeuroImage*, 70:340–355, April 2013.
 - [85] Mark Jenkinson, Christian F. Beckmann, Timothy E.J. Behrens, Mark W.

Woolrich, and Stephen M. Smith. Fsl. *NeuroImage*, 62(2):782–790, August 2012.

- [86] David P. Wipf, Julia P. Owen, Hagai T. Attias, Kensuke Sekihara, and Srikantan S. Nagarajan. Robust Bayesian estimation of the location, orientation, and time course of multiple correlated neural sources using MEG. *NeuroImage*, 49(1):641–655, January 2010.
- [87] Johanna M. Zumer, Hagai T. Attias, Kensuke Sekihara, and Srikantan S. Nagarajan. Probabilistic algorithms for meg/eeg source reconstruction using temporal basis functions learned from data. *NeuroImage*, 41(3):924–940, July 2008.
- [88] K. Jerbi, S. Baillet, J. C. Mosher, G. Nolte, L. Garnero, and R. M. Leahy. Localization of realistic cortical activity in meg using current multipoles. *NeuroImage*, 22(2):779–793, June 2004.
- [89] S S Dalal, J M Zumer, V Agrawal, K E Hild, K Sekihara, and S S Nagarajan. Nutmeg: a neuromagnetic source reconstruction toolbox. *Neurology & clinical neurophysiology : NCN*, 2004:52, 2004.
- [90] S Kirkpatrick, C D Gelatt, and M P Vecchi. Optimization by simulated annealing. *Science*, 220(4598):671–680, 1983.
- [91] Paul L. Nunez and Ramesh Srinivasan. A theoretical basis for standing and traveling brain waves measured with human eeg with implications for an integrated consciousness. *Clinical Neurophysiology: Official Journal of the International Federation of Clinical Neurophysiology*, 117(11):2424–2435, November 2006.
- [92] Sujith Vijayan, ShiNung Ching, Patrick L. Purdon, Emery N. Brown, and Nancy J. Kopell. Thalamocortical mechanisms for the anteriorization of alpha rhythms during propofol-induced unconsciousness. *The Journal of Neuroscience*, 33(27):11070–11075, July 2013.
- [93] A. van Rotterdam, F. H. Lopes da Silva, J. van den Ende, M. A. Viergever, and A. J. Hermans. A model of the spatial-temporal characteristics of the alpha rhythm. *Bulletin of Mathematical Biology*, 44(2):283–305, January 1982.
- [94] D.T.J. Liley, P.J. Cadusch, and M.P. Dafilis. A spatially continuous mean field theory of electrocortical activity. *Network: Computation in Neural Systems*, 13(1):67–113, January 2002.

- [95] Paul L. Nunez. A study of origins of the time dependencies of scalp eeg: I - theoretical basis. *IEEE Transactions on Biomedical Engineering*, BME-28(3):271–280, March 1981.
- [96] J. Daunizeau, O. David, and K. E. Stephan. Dynamic causal modelling: a critical review of the biophysical and statistical foundations. *NeuroImage*, 58(2):312–322, September 2011.
- [97] K J Friston, Katrin H Preller, Chris Mathys, Hayriye Cagnan, Jakob Heinze, Adeel Razi, and Peter Zeidman. Dynamic causal modelling revisited. *NeuroImage*, (February), 2017.
- [98] D. A. Pinotsis, E. Hansen, K. J. Friston, and V. K. Jirsa. Anatomical connectivity and the resting state activity of large cortical networks. *NeuroImage*, 65:127–138, 2013.
- [99] Adeel Razi, Joshua Kahan, Geraint Rees, and Karl J. Friston. Construct validation of a dcm for resting state fmri. *NeuroImage*, 106:1–14, 2015.
- [100] D. A. Pinotsis, J. P. Geerts, L. Pinto, T. H. B. FitzGerald, V. Litvak, R. Auksztulewicz, and K. J. Friston. Linking canonical microcircuits and neuronal activity: Dynamic causal modelling of laminar recordings. *NeuroImage*, 146:355–366, February 2017.
- [101] Jean Daunizeau, Stefan J. Kiebel, and Karl J. Friston. Dynamic causal modelling of distributed electromagnetic responses. *NeuroImage*, 47(2):590–601, 2009.
- [102] Hae Jeong Park, Karl J. Friston, Chongwon Pae, Bumhee Park, and Adeel Razi. Dynamic effective connectivity in resting state fmri. *NeuroImage*, 180(May 2017):594–608, 2018.
- [103] Frederik Van de Steen, Hannes Almgren, Adeel Razi, Karl Friston, and Daniele Marinazzo. Dynamic causal modelling of fluctuating connectivity in resting-state eeg. *NeuroImage*, 189:476–484, April 2019.
- [104] Maria Giulia Preti, Thomas AW Bolton, and Dimitri Van De Ville. The dynamic functional connectome: State-of-the-art and perspectives. *NeuroImage*, 160:41–54, October 2017.
- [105] Adeel Razi, Mohamed L. Seghier, Yuan Zhou, Peter McColgan, Peter Zeidman, Hae-Jeong Park, Olaf Sporns, Geraint Rees, and Karl J. Friston.

Large-scale dcms for resting-state fmri. *Network Neuroscience*, 1(3):222–241, October 2017.

- [106] Stefan Frässle, Ekaterina I. Lomakina, Adeel Razi, Karl J. Friston, Joachim M. Buhmann, and Klaas E. Stephan. Regression dcm for fmri. *NeuroImage*, 155(February):406–421, 2017.
- [107] Stefan Frässle, Ekaterina I. Lomakina, Lars Kasper, Zina M. Manjaly, Alex Leff, Klaas P. Pruessmann, Joachim M. Buhmann, and Klaas E. Stephan. A generative model of whole-brain effective connectivity. *NeuroImage*, 179(May):505–529, 2018.